Stem Cell Reports

Article

Surface Topography Guides Morphology and Spatial Patterning of Induced Pluripotent Stem Cell Colonies

Giulio Abagnale,[1] Antonio Sechi,[2,3] Michael Steger,[4] Qihui Zhou,[5] Chao-Chung Kuo,[2,6] Gülcan Aydin,[2,3] Carmen Schalla,[2,3] Gerhard Müller-Newen,[7] Martin Zenke,[2,3] Ivan G. Costa,[2,6,8] Patrick van Rijn,[5] Arnold Gillner,[4] and Wolfgang Wagner[1,2,*]

[1]Helmholtz Institute for Biomedical Engineering, Stem Cell Biology and Cellular Engineering, RWTH Aachen University Medical School, Pauwelsstrasse 20, 52074 Aachen, Germany
[2]Institute of Biomedical Engineering, Department of Cell Biology, RWTH Aachen University Medical School, 52074 Aachen, Germany
[3]Helmholtz Institute for Biomedical Engineering, RWTH Aachen University, 52074 Aachen, Germany
[4]Laser Technology (ILT), RWTH Aachen University, 52074 Aachen, Germany
[5]University of Groningen, University Medical Center Groningen, Biomedical Engineering Department-FB40, Groningen, the Netherlands
[6]IZKF Bioinformatics Research Group, RWTH Aachen University Medical School, 52074 Aachen, Germany
[7]Department of Biochemistry and Molecular Biology, RWTH Aachen University Medical School, 52074 Aachen, Germany
[8]Aachen Institute for Advanced Study in Computational Engineering Science (AICES), RWTH Aachen University, 52074 Aachen, Germany
*Correspondence: wwagner@ukaachen.de
http://dx.doi.org/10.1016/j.stemcr.2017.06.016

SUMMARY

The relevance of topographic cues for commitment of induced pluripotent stem cells (iPSCs) is largely unknown. In this study, we demonstrate that groove-ridge structures with a periodicity in the submicrometer range induce elongation of iPSC colonies, guide the orientation of apical actin fibers, and direct the polarity of cell division. Elongation of iPSC colonies impacts also on their intrinsic molecular patterning, which seems to be orchestrated from the rim of the colonies. BMP4-induced differentiation is enhanced in elongated colonies, and the submicron grooves impact on the spatial modulation of YAP activity upon induction with this morphogen. Interestingly, TAZ, a YAP paralog, shows distinct cytoskeletal localization in iPSCs. These findings demonstrate that topography can guide orientation and organization of iPSC colonies, which may affect the interaction between mechanosensors and mechanotransducers in iPSCs.

INTRODUCTION

Biophysical properties of the microenvironment, such as stiffness and topography, modulate differentiation and self-renewal ability of stem cells (Dalby et al., 2007; Engler et al., 2006). Structural features of the extracellular landscape can be mimicked *in vitro* by grooves and pores to control cell shape (Clark et al., 1991; Curtis and Varde, 1964; Dunn and Heath, 1976; Oakley and Brunette, 1993). Interaction of cells with surface topography results in forces that trigger intracellular responses such as proliferation and directed differentiation (Abagnale et al., 2015; Unadkat et al., 2011). Topographical cues are also relevant for the modulation of pluripotent stem cells (PSCs), which possess the ability to self-renew infinitely and have the potential to develop into every cell type of the human body (Takahashi et al., 2007). For example, it has been suggested that mechanical stimulation of embryonic stem cells (ESCs) can mimic the embryonic microenvironment and thereby influence the expression of pluripotency markers and cell fate decisions (Sun et al., 2012, 2014). Other reports showed that surface roughness affects the spreading of human ESCs (Chen et al., 2012) and that defined structures can drive lineage-specific differentiation (Lee et al., 2010; McFarlin et al., 2009; Pan et al., 2013). Nonetheless, a comparative study of how groove-ridge structures of

different sizes impact on induced PSCs (iPSCs) has so far not been reported. Moreover, it remains to be elucidated whether microtopographic stimuli affect the self-organization within iPSC colonies.

It has been recently described that expression of pluripotency factors is heterogeneous within iPSC colonies and that this heterogeneity may relate to the inherent diversity of human embryonic cells prior to gastrulation (Nazareth et al., 2013; Warmflash et al., 2014). A better understanding of how topography modulates the spatial organization of pluripotent cells is particularly relevant in early embryonic development, since it can drive the establishment of body axis and the formation of early anatomical structures (Keller et al., 2003). Changes in the geometry of pluripotent cells might alter such cell-cell interactions and the distribution of morphogenetic factors.

In mesenchymal stem cells the transcriptional coactivators YAP and TAZ function as mechanotransducers that translate physical stimuli, such as substrate elasticities and cellular density, into control of cellular growth and differentiation (Dupont et al., 2011; Halder et al., 2012). There is accumulating evidence that YAP and TAZ are generally involved in the regulation of cellular polarity and tissue homeostasis (Pan, 2007; Yu et al., 2015) and that they are crucial for the maintenance of pluripotency (Lian et al., 2010; Varelas et al., 2008). Nevertheless, it remains largely

CrossMark
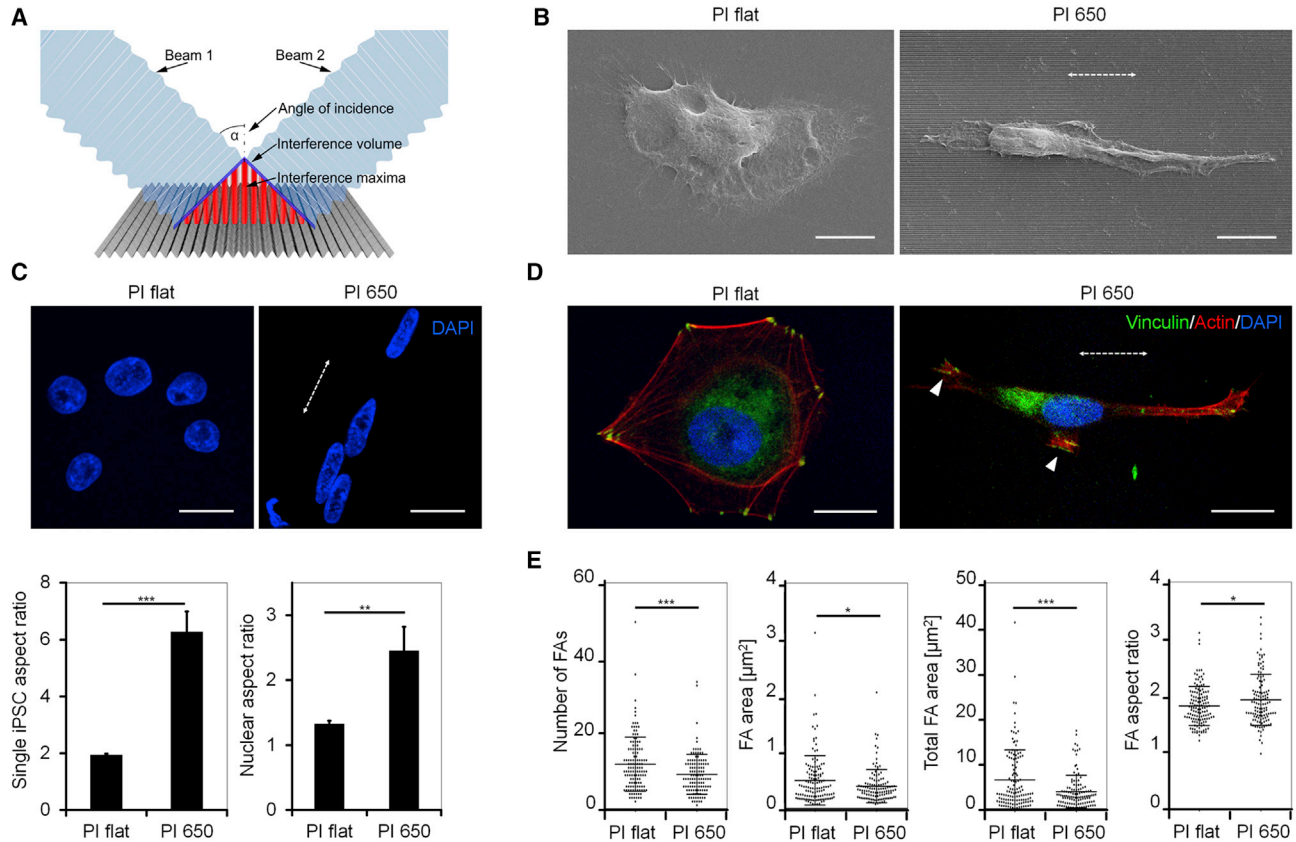
Figure 1. Submicron Grooves Affect Morphology of Single iPSCs

(A) Schematic representation of the two-beam interference structuring of grooves in polyimide with a periodicity of 650 nm (PI 650).

(B) Scanning electron microscopy images of individual iPSCs on flat polyimide and PI 650. Scale bars, 10 μm.

(C) Analysis of cellular and nuclear aspect ratios of individual iPSCs (n = 3 independent biological replica; **p < 0.01, ***p < 0.001, unpaired Student's t test). Scale bars, 20 μm.

(D) Confocal microscopy of actin (red) and vinculin (green) in single iPSCs. Arrowhead indicates elongated focal adhesions. Data are presented as mean ± SD. Scale bars, 20 μm.

(E) Analysis of focal adhesions on PI flat and PI 650 (n = 3 independent biological replica; *p < 0.05, ***p < 0.001, unpaired Student's t test).

The dotted white arrow always indicates the direction of the grooves; nuclei are stained with DAPI (blue).

unclear whether YAP and TAZ are directly involved in interaction with the cytoskeleton and recognition of topographic stimuli (Raghunathan et al., 2014). Moreover, YAP and TAZ might also be involved in regulation of cell-cell interaction and spatial conformation within iPSC colonies.

In this study we have used groove-ridge structures in the submicrometer range that were generated with laser interference technology to investigate the impact of surface topography on the morphology of individual iPSCs. Moreover, we have analyzed how surface topography impacts on the organization of iPSC colonies with regard to expression patterns of pluripotency markers, activity of YAP and TAZ, and differentiation in response to morphogen stimulation.

RESULTS

Laser-Ablated Submicron Grooves Induce Cellular and Nuclear Elongation of Individual iPSCs

In this work we employed multibeam laser interference to structure a polyimide foil with grooves with a periodicity of 650 nm and height of 200 nm (PI 650; Figure 1A). Polyimide is a biocompatible plastic polymer with good mechanical properties (Julien et al., 2011) and it is relatively resistant to higher temperatures, which makes it ideal for applications involving laser ablation. Atomic force microscopy (AFM) measurements of PI 650 validated the homogeneity of surface structures (Figures S1A and S1B). These substrates were highly anisotropic compared with the flat polyimide (PI flat), as indicated by contact angle
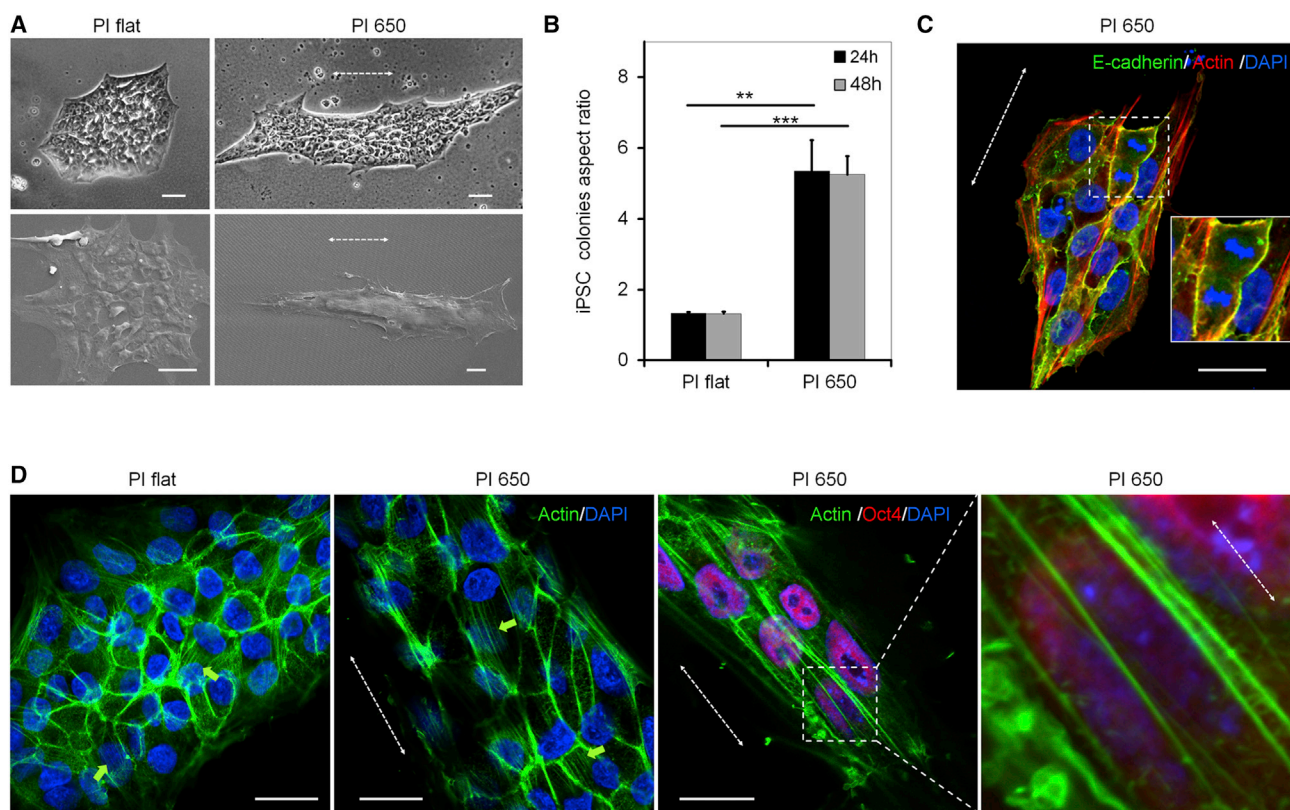
Figure 2. The Shape of iPSC Colonies Is Controlled by Submicron Topography

(A) Phase-contrast (top) and scanning electron microscopy images (bottom) of round and elongated iPSC colonies on PI flat and PI 650, respectively. Scale bars, 40 μm.

(B) Aspect ratio of the colonies either 24 or 48 hr after seeding (n = 3 independent biological replica; **p < 0.01, ***p < 0.001, unpaired Student's t test). Data are presented as mean ± SD.

(C) Representative images showing how topography directs the cell division plane perpendicularly to the submicron grooves; inlay highlights a mitosis. Scale bar, 40 μm.

(D) iPSCs have been stained for the actin cytoskeleton (green) and the pluripotency marker OCT4 (red) with DAPI (blue) as nuclear counterstaining. Green arrows highlight apical actin fibers. The dotted white arrows indicate the direction of the grooves. Scale bars, 20 μm.

measurements (Figure S1C) (Good, 1992). When single iPSCs were seeded on PI 650 they aligned parallel to the submicron structures and showed both cellular (Figure 1B) and nuclear elongation (Figure 1C). Fluorescence staining of individual iPSCs revealed an organized cytoskeleton with actin fibers extending along the grooves (Figure 1D). Vinculin staining indicated that focal adhesions are reduced in size and number on the structures, and possess increased aspect ratio compared with the flat material (Figure 1E). Thus, topography in the submicrometer range affects cellular and nuclear morphology of single iPSCs and modulates the focal adhesion compartment.

Surface Topography Impacts on the Morphology of iPSC Colonies by Directing the Cell Division Plane

iPSCs typically grow as tightly packed colonies, similar to epiblast cells within the developing embryo (Zou and Niswander, 1996). When seeded on flat polyimide substrates, iPSC colonies displayed the classical round morphology (Figure 2A) and were positive for OCT4 (*POU5F1*), NANOG, and E-cadherin (Figure S2A). Notably, on grooves with a periodicity of 650 nm these colonies acquired an elongated shape (Figures 2A and 2B), which did not interfere with the expression of these three pluripotency factors (Figure S2B). We also observed that the aspect ratio of elongated colonies remained constant, at about 6:1, as they grew over time, which was in a range similar to that previously observed for single iPSCs on PI 650 (Figure 2B). On the other hand, elongation parallel to grooves was scarcely observed for individual cells localized within iPSC colonies. Therefore, the mechanism of how an iPSC colony consisting of thousands of cells elongates cannot simply be attributed to elongation of individual cells. We hypothesized that the polarity of mitosis might

be influenced by surface topography. In fact the plane of cell division was found to be perpendicular to the direction of the grooves already at a single-cell level (Movie S1) and the same was observed within colonies (Figure 2C). Furthermore we observed apical actin fibers, which span above the nuclei and are orientated parallel to the submicron grooves (Figure 2D). On the other hand, the complex network of basal actin stress fibers and of actin filaments at cell-cell contacts did not seem to be modified by the structures (Figures S2C and S2D). These results indicate that topographic surface patterns can control the morphology of iPSC colonies by directing cell division planes and orientation of apical actin fibers.

Elongation of iPSC Colonies on Different Substrates and Structures

Subsequently, we analyzed whether similar effects on iPSC colonies were also observed on grooved structures of other dimensions or on different biomaterials. To this end, we generated submicron grooves featuring periodicities of 340 nm, 650 nm, and 1,400 nm on a polydimethylsiloxane (PDMS) by a strain-oxidation-release procedure with different air plasma oxidation times (Zhou et al., 2015). These materials are subsequently referred to as PDMS 340, PDMS 650, and PDMS 1400, respectively (Figures S3A–S3C). AFM measurements demonstrated that the periodicity of the structures was directly related to groove depth (Figure S3D). Single iPSCs seeded on PDMS 650 and PDMS 1400 clearly aligned along the patterns and displayed similar cellular and nuclear aspect ratios as previously observed on PI 650 (Figures 3A and 3C). Furthermore, the geometry of iPSC colonies was significantly altered by PDMS 650 and PDMS 1400, albeit to a lesser degree than on PI 650 (Figure 3B). Notably, on PDMS 340 neither individual iPSCs nor iPSC colonies were elongated and instead displayed a round shape as observed on flat PDMS. This similar threshold may indicate that the molecular processes for elongation of individualized cells and colonies are related.

Spatial Distribution of Pluripotency Markers Is Affected by Colony Geometry

Next we analyzed whether the geometry of iPSCs impacts on the distribution of pluripotency-related proteins within the colonies. As described before, iPSCs seeded on nonstructured polystyrene coverslips or flat polyimide display higher expression of pluripotency markers at the outer region of colonies compared with the center (Figure S4A). In iPSC colonies seeded on the PI 650, the expression pattern of OCT4 was elongated similarly to the morphology of the entire colony (Figure 4A). The same was true for NANOG, which is strongly expressed in cells at the rim of the colonies (Figures 4B and 4C). Furthermore, we observed a similar patterning in iPSC colonies seeded on flat and structured PDMS substrates (Figure S4B). These results indicate that the geometry of the colony is relevant for the self-organized heterogeneous expression of pluripotency factors. To rule out the possibility that these effects are only observed under specific culture conditions we performed additional experiments in TeSR-E8, a chemically defined culture medium specifically developed for culture of human PSCs (Chen et al., 2011). iPSCs cultured in TeSR-E8 displayed the same heterogeneous patterns of pluripotency markers as previously observed in iPS-Brew medium (Figure S4C).

The elongated morphology of iPSC colonies might also alter the response to biochemical signals. We have exemplarily analyzed the effect of bone morphogenetic proteins (BMPs) on the differentiation of iPSCs, since these factors play a crucial role in early embryonic differentiation (Richter et al., 2014). Exposure to BMP4 led to decreased expression of NANOG and OCT4, which started at the rim of colonies and successively proceeded toward the cells in the center. A similar differentiation pattern was also observed in TeSR-E8 medium (Figure S4D). Importantly, in elongated colonies the loss of these pluripotency markers was more pronounced compared with round ones (Figures 4B and 4C). Moreover, qRT-PCR analysis confirmed that OCT4 and NANOG are downregulated faster on PI 650 compared with PI flat after stimulation with BMP4 (Figure 4D). Our data indicate that changes in colony morphology, elicited by submicron surface topography, impact on differentiation patterns in response to morphogens.

We followed the hypothesis that submicron topography directly modulates the transcriptional program of iPSCs. Single iPSCs were seeded on either flat or structured polyimide, and gene expression profiles were compared after 3 days. None of the genes revealed significant differential gene expression when cells were kept under culture conditions that maintained pluripotency (Figure 5A). Additionally we analyzed gene expression changes during 2 weeks of multilineage differentiation. In the course of differentiation many genes were significantly up- and downregulated, and this was more pronounced on PI flat than on PI 650 (Figures S5A–S5C). Furthermore, pairwise comparison of iPSCs that were differentiated on structured versus flat biomaterials revealed significant downregulation of 80 genes and upregulation of 4 genes (adjusted p < 0.05; Figures 5B and 5C; Table S1). Gene Ontology analysis demonstrated that differentially expressed genes were particularly enriched in the categories of extracellular matrix remodeling and tissue morphogenesis (Figure S5D). Of note, the biggest fold change on PI 650 versus PI flat after differentiation was observed in *ANKRD1*, which is a well-characterized readout of YAP/TAZ activity (Aragona et al., 2013).
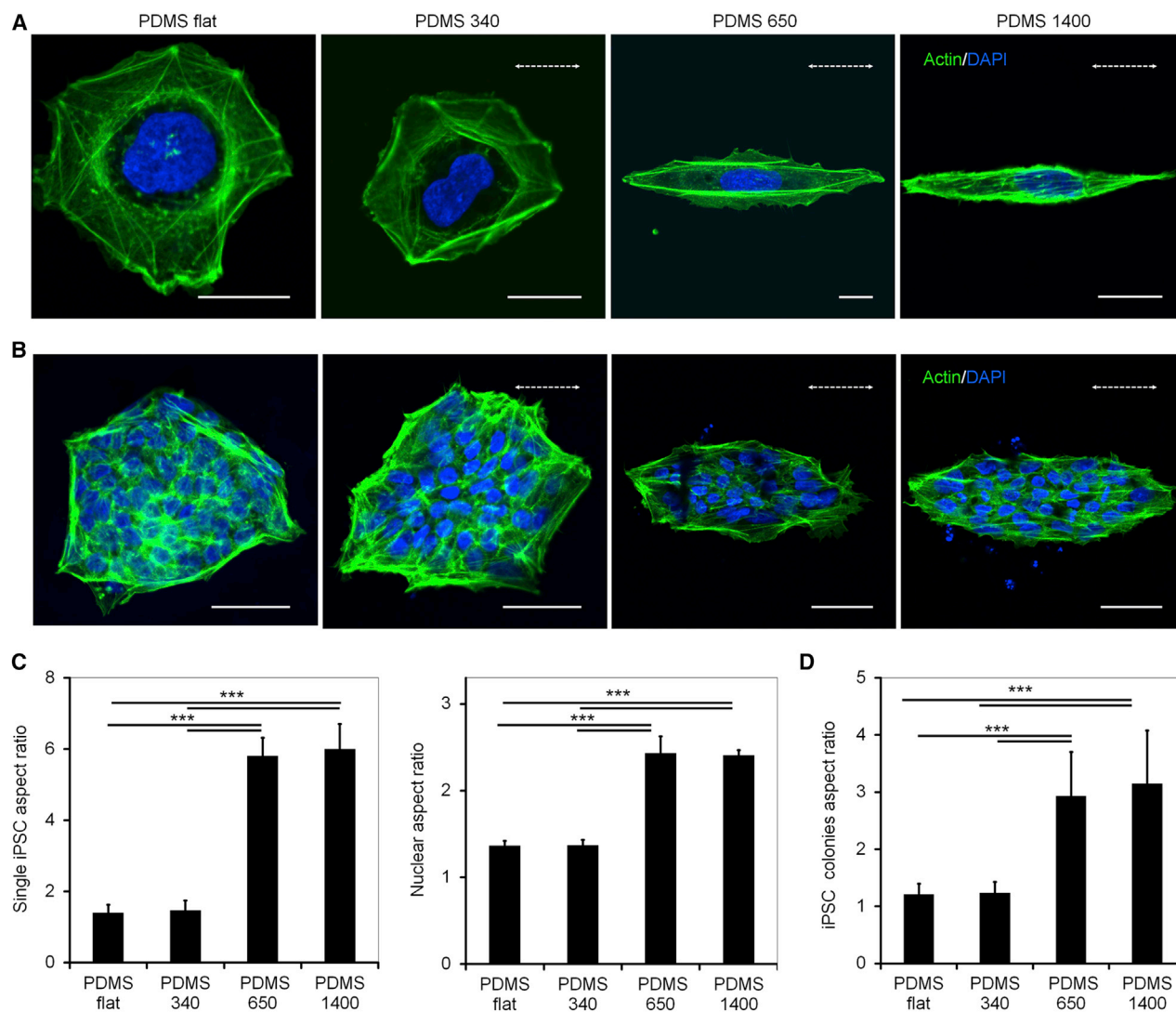
Figure 3. Structures with Diverse Size Induced Distinct Morphological Changes in iPSCs

(A and B) Confocal microscopy images of single iPSCs (A) and iPSC colonies (B) seeded on PDMS substrates that were structured with grooves of different periodicities. Cells were stained for actin (green) and nuclei (blue). The dotted white arrows indicate the direction of the submicron grooves. Scale bars, 20 μm in (A) and 50 μm in (B).

(C and D) Analysis of nuclear and cellular aspect ratio for single iPSCs (C) and whole iPSC colonies (D) when seeded on the PDMS submicron-grooved substrates. Data are presented as mean ± SD (n = 3 independent biological replicates, ***p < 0.001).

YAP and TAZ Show Distinct Localizations within iPSC Colonies

The transcriptional coactivators YAP and TAZ play important roles for mechanotransduction (Dupont et al., 2011; Kanai et al., 2000). Nonetheless, little is known about their function in pluripotent cells. Within iPSC colonies YAP and TAZ are predominantly localized in the nucleus, which may reflect their activity as transcription factors. Notably, during mitosis TAZ was tightly associated with condensed chromatin, whereas YAP was predominantly confined to the cytoplasm, and this was consistently observed in more than 250 cell divisions analyzed (Figures 6A, S6A, and S6B). Furthermore, we report that TAZ, but not YAP, was associated with filamentous structures that might resemble actin fibers (Figures 6B and S6C). Such TAZ localization was particularly evident in cells at the outer rim of iPSC colonies (Figure 6C). In contrast, YAP did not co-stain with cytoskeletal structures. These results indicate that the two paralogs TAZ and YAP might exert different functions.

We subsequently wanted to further investigate the filamentous localization of TAZ. Previous studies have described such localization at cell-cell junctions (Zhao
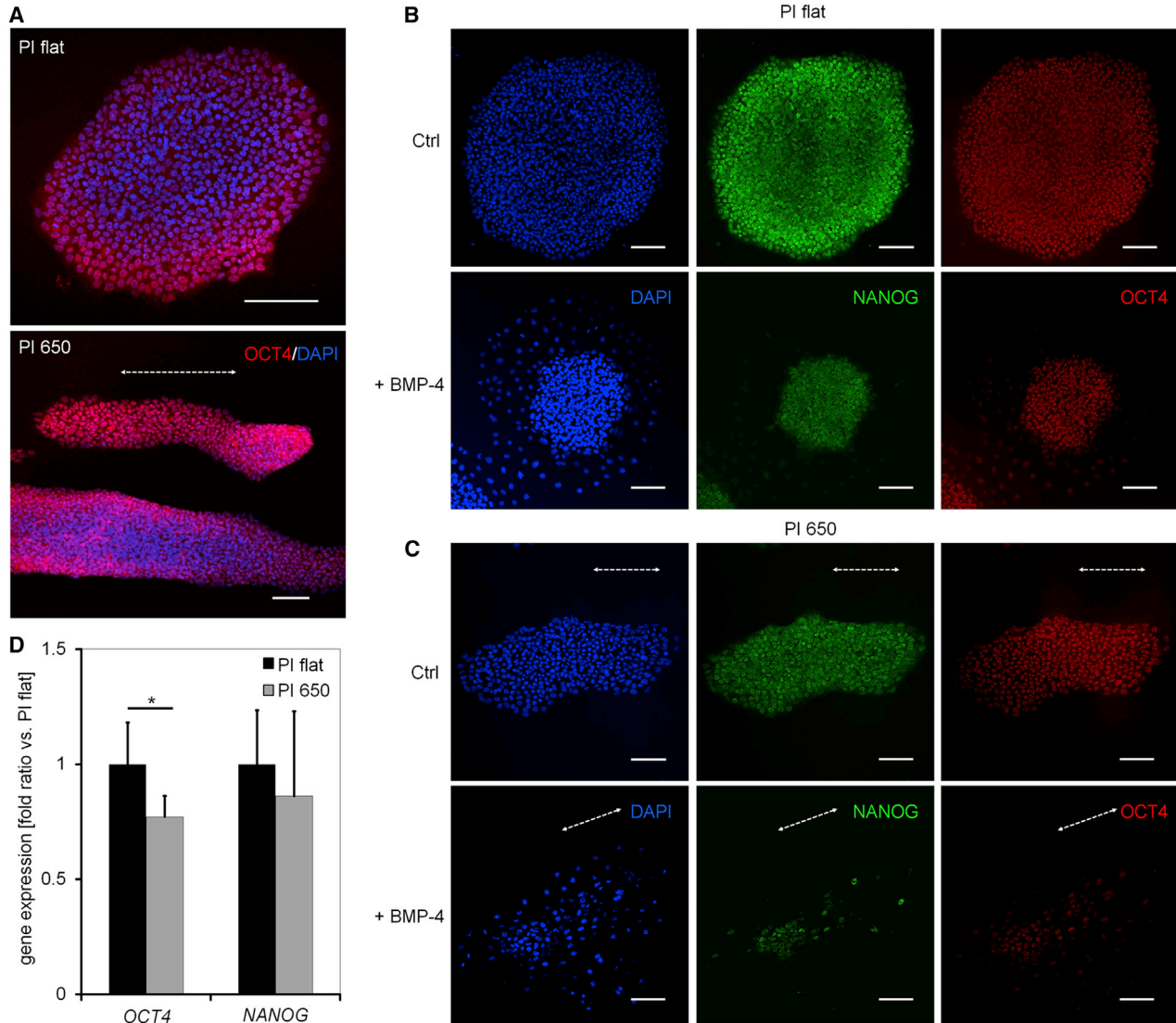
**Figure 4. Submicron Structures Affect Patterning of iPSC Colonies**

(A) Spatial heterogeneity of OCT4 (red) expression in round versus elongated iPSC colonies as shown by immunofluorescence staining. Scale bars, 100 μm.

(B and C) Confocal microscopy images showing of the distribution the pluripotency markers NANOG (green) OCT4 (red) in pluripotent colonies and upon induction with BMP4 for 48 hr on flat (B) and grooved polyimide (C). The dotted white arrows indicate the direction of the grooves; nuclei are stained with DAPI (blue). Scale bars, 100 μm.

(D) qRT-PCR analysis of expression levels of *OCT4* and *NANOG* in iPSCs after exposure to 50 ng/μL BMP4 for 17 hr. Data are presented as mean ± SD. *GAPDH* was used as housekeeping gene (n = 3 independent biological replicates, *p < 0.05).

et al., 2011), whereas we also observed prominent TAZ expression close to focal adhesions of individual iPSCs (Figure 6D) and at the tip of actin filaments (Figure 6E; Movie S2). Western blot analysis validated that TAZ was present in the protein fraction that is bound to actin (Figure 6F). To gain additional insight into the subcellular localization of TAZ, we overexpressed a TAZ-GFP fusion protein in iPSCs and analyzed it by total internal reflection fluorescence (TIRF) microscopy. This analysis confirmed that TAZ is localized in filaments within 70 nm of the basal plasma membrane (Movie S3) at a region where recognition of topographic stimuli takes place (Kanchanawong et al., 2010). Furthermore, the GFP-tagged TAZ revealed transient association with condensed chromatin during mitosis, as previously observed in immunofluorescence microscopy (Movie S4). These results indicate that TAZ can interact
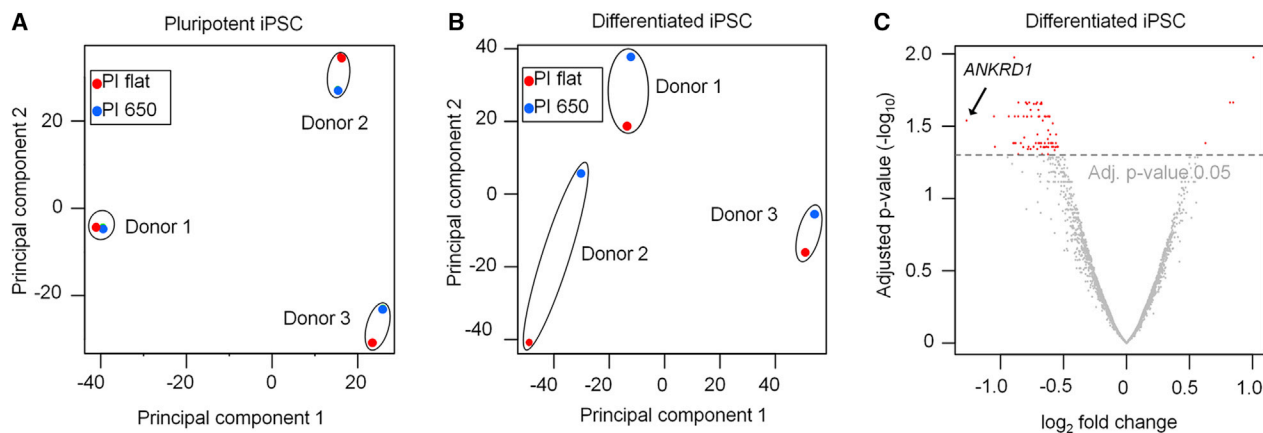
Figure 5. Genome-wide Analysis of the iPSC Transcriptome on Flat and Structured Polyimide

(A) Principal component analysis (PCA) based on gene expression data of iPSCs in pluripotent state. The iPSC lines cluster together, whereas surface topography has little impact (n = 3 independent biological replicates).

(B) PCA based on gene expression data of iPSCs after 2 weeks of differentiation on either PI flat or PI 650: cells cultured on the submicron structures have higher PC2 scores than cells of the same donor cultured on flat surfaces (n = 3 independent biological replicates).

(C) Differentiation iPSCs on the two substrates resulted in significant differences of gene expression: 80 are downregulated and 4 are upregulated on PI 650 versus PI flat (n = 3 independent biological replicates; adjusted p < 0.05, paired limma t test).

with the actin cytoskeleton and components of focal adhesions. Interestingly, we observed that vinculin was partly detected in the nuclei of iPSCs. This was observed by immunostaining and validated by western blot analysis of subcellular fractions of iPSCs (Figures S6D and S6E). It is therefore conceivable that nuclear transfer of vinculin is due to its association with TAZ.

YAP, on the other hand, seemed to modulate BMP4-induced differentiation in relation to the spatial organization of the colonies. Upon BMP4 exposure, YAP was predominantly confined to the cytoplasm in cells of the inner portion of the colonies (Figure 6G) while in cells of the outer rim it was exclusively nuclear. This differential localization of YAP in the middle versus outside of the colonies was also validated in TeSR-E8 medium (Figure S6F). Morphological changes of iPSC colonies that were triggered by surface topography were also reflected in spatial expression of YAP: on polyimide with submicron structures the stimulation with BMP4 resulted in an elongated inner portion of the colony where YAP was translocated to the cytoplasm. Hence, surface topography may, either directly or indirectly, influence localization of YAP in response to morphogens, depending on the position of the target cells within the colony.

DISCUSSION

Surface topography guides not only morphology and migration of individual iPSCs but also impacts on the architecture and self-organization of iPSC colonies. Elongated

colonies have distinct expression patterns of pluripotency markers and are more susceptible to morphogen-induced differentiation. In principle, the grooves might directly influence cellular differentiation or might exert indirect effects via reorganization of cell-cell interactions.

Different microfabrication processes can be employed to generate highly reproducible substrates with precise topographies in the submicrometer range. Laser technology, and in particular multibeam interference, is used to ablate the surface of a substrate and allows the direct structuring of most types of materials. In contrast to common laser techniques, laser interference is not limited by light diffraction and hence enables generation of subwavelength structures (Burrow and Gaylord, 2011). Production of submicron grooves in pre-strained PDMS substrates by air plasma treatment followed by their release is relatively easy to implement and is cost effective (Zhou et al., 2015). Furthermore, homogeneous patterning of the entire surface is facilitated and gradients can be obtained. The technique is initially limited to PDMS substrates, but it is possible to translate the structures into other materials by imprinting lithography (Zhou et al., 2016). On the other hand, the wrinkle or grating structures are less controlled and are more susceptible to batch-to-batch variation than surface structures generated by multibeam interference.

We demonstrate that submicron topography induces an increase in the aspect ratio of individual iPSCs and of iPSC colonies, and this was observed on polyimide and PDMS. Notably, elongation of individual iPSCs was similar in PI 650 and PDMS 650. However, iPSCs do not normally grow as dissociated cells; they persist in this state only for
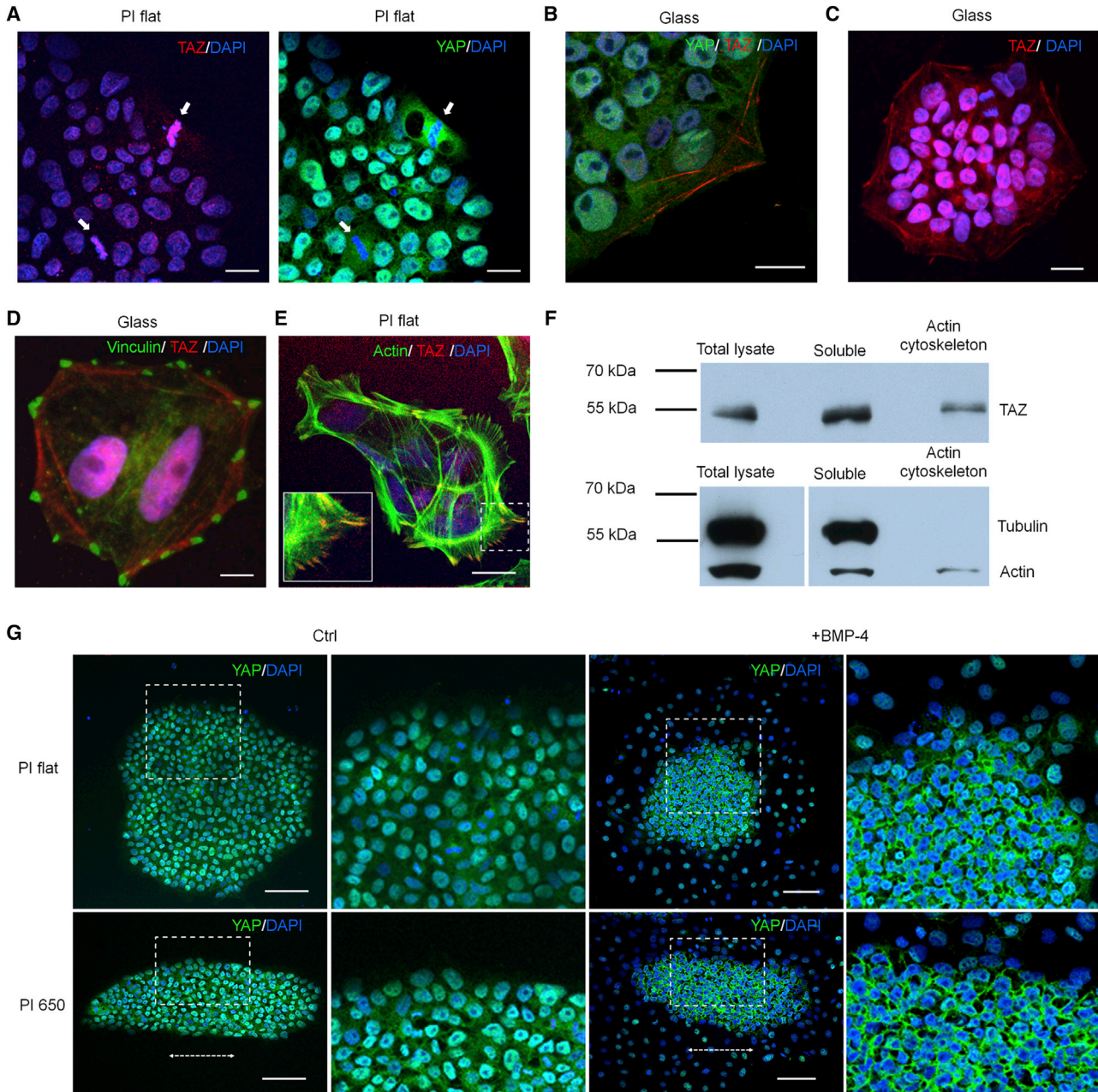
Figure 6. Distribution of YAP and TAZ in iPSCs

(A) Immunofluorescence images showing distinct distribution of YAP (green) and TAZ (red) in dividing iPSCs (white arrows). Scale bars, 20 μm.

(B) Immunostainings showing the presence of the mechanotransducer TAZ (red) but not of YAP (green) in filamentous structures similar to stress fibers. Scale bar, 20 μm.

(C) Confocal image displaying stronger cytoskeletal localization for TAZ (red) at the rim of an iPSC colony. Scale bar, 20 μm.

(D) Immunofluorescence image showing TAZ filaments (red) spanning between focal adhesion sites (green). Scale bar, 10 μm.

(E) Confocal microscopy image of iPSCs showing TAZ (red) localization at the tip of the actin fibers (green). Scale bar, 20 μm.

(F) Western blot shows that TAZ is present in the protein fraction of iPSCs associated to the actin cytoskeleton.

(G) Immunostaining showing YAP (green) localization in iPSCs before and after induction with BMP4 on both flat and grooved polyimide. Nuclei are always counterstained with DAPI (blue), and the dotted arrows indicate the direction of the grooves. Scale bars, 100 μm.

few hours before they undergo mitosis and grow eventually into a colony (Movie S1). The higher aspect ratio of individualized iPSCs might impact on their actin-myosin contractility, which was shown to be responsible for reduced viability of dissociated pluripotent cells (Chen et al., 2010). In contrast, elongation of colonies may rather be attributed to defined cell division planes and apical actin fibers, although the molecular mechanisms for mechanosensing might be the same. On PDMS 340 we did not observe elongation of individual iPSCs or colonies. It needs to be taken into account that for cell-substrate interactions not only the periodicity of the structures, but also their depth, is relevant (Lamers et al., 2010; Wojciak-Stothard et al., 1996) as well as the elastic modulus of the material and its chemical composition (Discher et al., 2005). Perhaps the periodicity of 340 nm is below the threshold that can be sensed by the cells, or the grooves are too shallow to be detected (about 13 nm depth). Either way, neither individualized iPSCs nor iPSC colonies seem to be affected by these very small structures. The height of PDMS 650 patterns is about 60–70 nm, which is in a range similar to the diameters of collagen fibers (Hulmes, 2002; Schmitt et al., 1942); therefore, the extracellular matrix components may also feature similar topography. Furthermore, as mechanical stress is generated not only at the cell-material interface but also at cell-cell contacts (Chu et al., 2004), the effects of surface topography are also influenced by the interplay of cells on structured materials. Traction forces between neighboring cells might mitigate the morphological changes elicited by the grooves. In fact, cells within the colonies display a more round shape, whereas individual cells revealed extensive elongation along the submicron grooves.

The higher expression of pluripotency factors at the outer region of iPSC colonies was similarly observed in two different culture media and on three different materials: polystyrene, polyimide, and PDMS. Thus, this patterning appears to be orchestrated by cell-cell interaction, rather than by material properties such as surface chemistry or elasticity. Hence, it would be interesting to compare gene expression at different regions of the same colony by laser microdissection to better understand the molecular differences. Surface topography did not interfere with pluripotency of iPSC colonies, and we did not observe significant gene expression changes when individual iPSCs were seeded on either PI flat or PI 650. These results indicate that surface structures have relatively little direct impact on the molecular makeup of iPSCs while they are in a pluripotent state.

Differentiation of iPSC colonies seems to be initiated at the rim, where the cells are more likely to undergo reversible epithelial-to-mesenchymal transition compared with those at the center (Chen et al., 2014). It has to be taken into account that culture media have a significant impact on cellular behavior. In fact, other authors reported that BMP4-induced differentiation of human ESCs varies under different defined culture conditions for pluripotent cells (Yu et al., 2011). However, when comparing two different commercially available media for the maintenance of iPSCs, we did not find differences in the intrinsic patterning of the colonies nor in the loss of pluripotency markers initiated by BMP4 treatment. This finding seems to be consistent with those of other studies (Warmflash et al., 2014). In elongated colonies the rim region is larger as compared with round colonies of comparable size, and this might be the reason why morphogen-driven differentiation was faster in elongated colonies. Alternatively cell-cell interactions, e.g., via paracrine effects, might affect differentiation kinetics. This finding is in line with a recent study that described self-organization of cellular architecture at different developmental stages of human blastocysts (Deglincerti et al., 2016). Taken together, it appears likely that our submicron grooves do not directly influence differentiation but rather control the spatial conformation of iPSC colonies, which then impacts on cell fate decisions.

Several studies indicated that YAP plays an important role during lineage specification (Pan, 2010). It is intriguing that upon BMP4 stimulation YAP reveals nuclear localization at the rim, whereas it is rather cytoplasmic at the center of differentiating iPSC colonies. Thus, it is conceivable that the different regions are more prone to differentiate into one or the other lineage. YAP might translate positional information in human pluripotent cells, similarly to what was previously observed in murine models (Nishioka et al., 2009). Furthermore, YAP was reported to be localized in the nucleus within the inner cell mass of human blastocytes and functions as important regulator of naive state (Qin et al., 2016). On the other hand TAZ, a YAP paralog, displayed unique spatial expression, which might indicate a different function: we describe that TAZ strongly co-localizes with actin filaments and cell-material adhesion sites in iPSCs. It is therefore conceivable that TAZ shuttles between the molecular machinery that recognizes topographical cues and the nucleus, where these stimuli are translated into the expression of specific genes.

In conclusion, surface topography in the submicrometer range affects morphology and migration of individual iPSCs. Furthermore, such structures guide the organization of iPSC colonies by directing apical actin fibers and cell division planes. Our work indicates that this indirect impact on cell-cell interaction and self-organization within iPSC colonies is relevant for differentiation processes and seems to involve the YAP/TAZ pathways. Tailored biomaterials may therefore mimic topographic cues of the extracellular matrix to modulate cell-cell interaction and thereby support directed differentiation.

EXPERIMENTAL PROCEDURES

Two-Beam Laser Interference

Polyimide substrates (PI-2611, HD Microsystems) with a sample size of 20 × 20 mm were structured using a diode pumped Q301-HD Nd:YAG laser (JDS Uniphase) operating at a wavelength of 355 nm with a pulse duration of 38 ns and a coherence length of 5.2 mm, as described previously (Abagnale et al., 2015). The laser output is measured with a QE12LP-S-MP energy detector (Gentec Electro Optics) and a beam profiler (Ophir-Spiricon), while the ablation area is measured by a VKX 5000 digital microscope (Keyence). The effective interference contrast was determined to be 0.72 (Steger et al., 2014). The incidence angle of beams was set to 15.87° relative to surface normal, which results in periodicity of the interference pattern of 650 nm (Steger et al., 2013). The topography of generated structures was assessed by a Rados N8 atomic force microscope (Bruker Corporation).

Generation and Characterization of the PDMS Substrates

PDMS substrates were generated as described previously (Zhou et al., 2015, 2016). In brief, PDMS pre-polymer and crosslinker (Sylgard 184; Dow Corning) were mixed in 10:1 ratio (w/w). PDMS substrates (9.5 × 9.5 cm, ~1.5 mm thickness) were then stretched uniaxially to 130% of their original length. The samples were oxidized between 60 and 500 s in air plasma under pressure of 14 torr (0.2 mbar; Plasma Activate Flecto 10 USB). Removal of strain evoked wrinkle formation of different periodicities and height depending on the oxidation time. All samples were post-treated with air plasma for 10 min to ensure equal oxidation and Young's modulus values (62 MPa). AFM profiles were obtained using a Nanoscope V Dimension 3100 microscope (Veeco), whereas the stiffness analysis was performed on a Catalyst Nanoscoop V instrument (Bruker). Bruker SCANASYST-AIR (0.4 N m^{-1}) and NP (0.017 N m^{-1}) cantilevers made from silicon nitride with silicon tips were used before each measurement.

Induced Pluripotent Stem Cells

In this work we used two iPSC lines derived from bone marrow-derived human mesenchymal stromal cells, and one iPSC line obtained from human dermal fibroblasts (Willmann et al., 2013). Pluripotency was assessed by immunophenotypic analysis, multi-lineage differentiation, and Epi-Pluri-Score (Lenz et al., 2015). iPSCs were cultured in 6-well plates coated with 0.5 μg/cm^2 of vitronectin (STEMCELL Technologies) and maintained in iPS-Brew medium (Miltenyi Biotec) supplemented with 1% penicillin/streptomycin (Life Technologies). Furthermore, we performed additional experiments with TeSR E8 (STEMCELL) to exclude that the observations were only related to specific culture conditions. iPSC differentiation was induced by addition of 50 ng/mL BMP4 (Miltenyi Biotec) for 48 hr.

Immunofluorescence Staining

Samples were fixed with 4% paraformaldehyde (Carl Roth) for 20 min, blocked with 1% BSA in Tris-buffered saline for 40 min, washed three times in 1× PBS (Life Technologies), and stained with primary antibody (OCT4, sc9081, Santa Cruz Biotechnology;

Nanog, ab62734, Abcam; E-cadherin, AF648, R&D Systems; YAP, sc101199, Santa Cruz; TAZ, ab84927, Abcam) overnight at 4°C. All antibodies were diluted 1:50 in PBS containing 0.1% Triton X-100. Subsequently the samples were washed three times with PBS and incubated with secondary antibodies (Alexa Fluor, Life Technologies; diluted 1:200 in PBS containing 0.1% Triton X-100 and DAPI [Molecular Probes, 1:1,000 dilution]) for 1 hr.

Microscopy and Image Analysis

Acquisition of immunofluorescence images was performed with an LSM 710 confocal microscope (Carl Zeiss). Aspect ratio analysis was performed with ImageJ (https://imageJ.nih.gov./ij/) by dividing the major axis by the minor axis of cells and nuclei. For focal adhesion analysis, images of vinculin staining were converted to binary images in ImageJ and then analyzed with the SOFAST plugin. Phase-contrast images were obtained using an EVOS fl microscope (Life Technologies). Scanning electron microscopy images of iPSCs were acquired with an LEO 1455 EP microscope (Carl Zeiss) on fixed cells (4% paraformaldehyde) that were coated with a gold layer using a Sputter Coater 108auto (Cressington Scientific) as described previously (Abagnale et al., 2015). Time-lapse movies were taken with an Axio Observer Z1 inverted microscope (Carl Zeiss) equipped with heating stage and CO_2 controller. For TIRF (Movie S3), GFP-TAZ was imaged using a 100×/1.46 numerical aperture (NA) objective. GFP was excited using 488-nm laser line at 10% of its nominal output power. The depth of the evanescent field was about 70 nm. Images were acquired every 15 s using a CCD camera (Evolve; Photometrics) driven by ZEN software (Carl Zeiss). For time-lapse movies (Movie S4), GFP-TAZ was imaged using a 20×/0.5 NA objective. GFP was excited using an HXP 120 illumination source in combination with filter set 52 (Carl Zeiss). Images were acquired every minute using a CCD camera (Evolve; Photometrics) driven by ZEN software (Carl Zeiss).

Gene Expression Profiling

iPSC colonies were dissociated into single cells with Accutase (Innovative Cell Technologies) and then either cultured for 3 days on vitronectin coated materials in iPSCs culture medium or for 14 days in medium that supports their spontaneous differentiation (KO-DMEM 80%, serum replacement 20%, 2 mM L-glutamine, 100 U/mL penicillin-streptomycin, non-essential amino acids 1%; all reagents from Life Technologies). Subsequently the cells were harvested and total RNA was isolated using a Nucleospin RNA plus kit (Macheray Nagel). Quality of RNA was assessed with a NanoDrop 2000 spectrophotometer (Thermo Scientific). Hybridization on Gene Chip Human Transcriptome Arrays 2.0 (Affymetrix) was performed at Life&Brain (Bonn, Germany) according to the manufacturer's guidelines. We performed normalization by Robust Multichip Average algorithm (RMA; oligo package in R) and differential expression was analyzed with paired limma t test (Ritchie et al., 2015). To this end, we focused on gene with higher variance than 0.05 across different arrays, and did multiple-test correction by Benjamini-Hochberg method with cutoff of adjusted p value of <0.05. Gene ontology analysis was performed with the gProfile tool (Reimand et al., 2016). The microarray data are accessible in the NCBI GEO (http://www.ncbi.nlm.nih.gov/geo/) through accession number GEO: GSE84848.

qRT-PCR Analysis for the Expression of Pluripotency Markers

RNA was isolated with TRIzol reagent (Sigma-Aldrich) and its quality assessed with a NanoDrop ND2000 (Thermo Scientific). cDNA was generated with a High Capacity cDNA Reverse Transcription Kit (Applied Biosystems, Darmstadt, Germany). Semi-quantitative RT-PCR was carried out with power SYBR Green master mix (Applied Biosystems) for the following genes: *OCT4* (forward 5′-GGG GGT TCT ATT TGG GAA GGT A-3′, reverse 5′-ACC CAC TTC TGC AGC AAG GG-3′), *NANOG* (forward 5′-CAG AAG GCC TCA GCA CCT AC-3′, reverse 5′-ATT GTT CCA GGT CTG GTT GC-3′), and *GAPDH* (forward 5′-GAA GGT GAA GGT CGG AGT C-3′, reverse 5′-GAA GAT GGT GAT GGG ATT TC-3′).

Western Blotting

Cytoplasmic and nuclear fractions were prepared as previously described in detail (Suzuki et al., 2010). In brief, cells were washed with PBS (37°C) and lysed for 10 min on ice with cytoskeleton lysis buffer (CLB; 0.5% Triton X-100, 10 mM 1,4-piperazine-diethanesulfonic acid [pH 7.4], 150 mM NaCl, 5 mM EGTA, 5 mM glucose, 5 mM magnesium chloride, supplemented with 0.5 mM sodium fluoride, 1 mM sodium orthovanadate, and protease inhibitors cocktail). Afterward the Triton soluble fraction, corresponding to the cytosolic fraction, was collected and clarified at $10,000 \times g$ for 10 min at 4°C. The cell monolayer was then washed twice with ice-cold cell lysis buffer and incubated with RIPA buffer for 15 min on ice. After the cells were scraped off, the RIPA buffer (Triton-insoluble or cytoskeletal fraction) was clarified at $12,000 \times g$ for 10 min at 4°C. Both fractions were resolved by SDS-PAGE and probed by western blotting with antibodies against TAZ (1:1,000; V386, Cell Signaling Technology), actin (1:10,000; clone AC-74, Sigma-Aldrich), tubulin (clone YL1/2 [Gamper et al., 2016]), and vinculin (1:1,000; clone hVin-1, Sigma-Aldrich).

Generation of TAZ-GFP Fusion Protein

The open reading frame (ORF) of human *WWTR1* (TAZ) was amplified by PCR from the 3xFLAG pCMV5-TOPO TAZ WT plasmid (Addgene; plasmid #24809) using the following primers: forward 5′-AAT TAG GAA TTC CAT GAA TCC GGC CTC GGC GCC C-3′ (to introduce an EcoRI site) and reverse 5′-GAT GGA TCC CTT ACA GCC AGG TTA GAA AGG GCT C-3′ (to introduce a BamHI site). The amplified product was cloned into the pWPXL-GFP plasmid (kindly provided by Trono Lab, EPFL, Lausanne, Switzerland) to generate WWTR1-GFP. The integritiy of the ORF was verified by DNA sequencing. The pWPXL WWTR1-GFP plasmid was then transfected into HEK293T cells together with pMD2G and psPAX vectors (kindly provided by Trono Lab) to produce lentiviral particles that were used to infect iPSCs. GFP-positive clones were then manually picked and expanded.

SUPPLEMENTAL INFORMATION

Supplemental Information includes six figures, one table, and four movies and can be found with this article online at http://dx.doi.org/10.1016/j.stemcr.2017.06.016.

REFERENCES

Abagnale, G., Steger, M., Nguyen, V.H., Hersch, N., Sechi, A., Joussen, S., Denecke, B., Merkel, R., Hoffmann, B., Dreser, A., et al. (2015). Surface topography enhances differentiation of mesenchymal stem cells towards osteogenic and adipogenic lineages. Biomaterials *61*, 316–326.

Aragona, M., Panciera, T., Manfrin, A., Giulitti, S., Michielin, F., Elvassore, N., Dupont, S., and Piccolo, S. (2013). A mechanical checkpoint controls multicellular growth through YAP/TAZ regulation by actin-processing factors. Cell *154*, 1047–1059.

Burrow, G.M., and Gaylord, T.K. (2011). Multi-beam interference advances and applications: nano-electronics, photonic crystals, metamaterials, subwavelength structures, optical trapping, and biomedical structures. Micromachines *2*, 221.

Chen, G., Hou, Z., Gulbranson, D.R., and Thomson, J.A. (2010). Actin-myosin contractility is responsible for the reduced viability of dissociated human embryonic stem cells. Cell Stem Cell *7*, 240–248.

Chen, G., Gulbranson, D.R., Hou, Z., Bolin, J.M., Ruotti, V., Probasco, M.D., Smuga-Otto, K., Howden, S.E., Diol, N.R., Propson, N.E., et al. (2011). Chemically defined conditions for human iPSC derivation and culture. Nat. Methods *8*, 424–429.

Chen, W., Villa-Diaz, L.G., Sun, Y., Weng, S., Kim, J.K., Lam, R.H., Han, L., Fan, R., Krebsbach, P.H., and Fu, J. (2012). Nanotopography influences adhesion, spreading, and self-renewal of human embryonic stem cells. ACS Nano *6*, 4094–4103.

Chen, K.G., Mallon, B.S., Johnson, K.R., Hamilton, R.S., McKay, R.D., and Robey, P.G. (2014). Developmental insights from early mammalian embryos and core signaling pathways that influence human pluripotent cell growth and differentiation. Stem Cell Res. *12*, 610–621.

Chu, Y.S., Thomas, W.A., Eder, O., Pincet, F., Perez, E., Thiery, J.P., and Dufour, S. (2004). Force measurements in E-cadherin-mediated cell doublets reveal rapid adhesion strengthened by actin cytoskeleton remodeling through Rac and Cdc42. J. Cell Biol. *167*, 1183–1194.

Clark, P., Connolly, P., Curtis, A.S., Dow, J.A., and Wilkinson, C.D. (1991). Cell guidance by ultrafine topography *in vitro*. J. Cell Sci. *99* (Pt 1), 73–77.

Curtis, A.S., and Varde, M. (1964). Control of cell behavior: topological factors. J. Natl. Cancer Inst. *33*, 15–26.

Dalby, M.J., Gadegaard, N., Tare, R., Andar, A., Riehle, M.O., Herzyk, P., Wilkinson, C.D.W., and Oreffo, R.O.C. (2007). The control of human mesenchymal cell differentiation using nanoscale symmetry and disorder. Nat. Mater. *6*, 997–1003.

Deglincerti, A., Croft, G.F., Pietila, L.N., Zernicka-Goetz, M., Siggia, E.D., and Brivanlou, A.H. (2016). Self-organization of the in vitro attached human embryo. Nature *533*, 251–254.

Discher, D.E., Janmey, P., and Wang, Y.L. (2005). Tissue cells feel and respond to the stiffness of their substrate. Science *310*, 1139–1143.

Dunn, G.A., and Heath, J.P. (1976). A new hypothesis of contact guidance in tissue cells. Exp. Cell Res. *101*, 1–14.

Dupont, S., Morsut, L., Aragona, M., Enzo, E., Giulitti, S., Cordenonsi, M., Zanconato, F., Le Digabel, J., Forcato, M., Bicciato, S., et al. (2011). Role of YAP/TAZ in mechanotransduction. Nature *474*, 179–183.

Engler, A.J., Sen, S., Sweeney, H.L., and Discher, D.E. (2006). Matrix elasticity directs stem cell lineage specification. Cell *126*, 677–689.

Gamper, I., Fleck, D., Barlin, M., Spehr, M., El Sayad, S., Kleine, H., Maxeiner, S., Schalla, C., Aydin, G., Hoss, M., et al. (2016). GAR22-beta regulates cell migration, sperm motility, and axoneme structure. Mol. Biol. Cell *27*, 277–294.

Good, R.J. (1992). Contact angle, wetting, and adhesion: a critical review. J. Adhes. Sci. Technol. *6*, 1269–1302.

Halder, G., Dupont, S., and Piccolo, S. (2012). Transduction of mechanical and cytoskeletal cues by YAP and TAZ. Nat. Rev. Mol. Cell Biol. *13*, 591–600.

Hulmes, D.J.S. (2002). Building collagen molecules, fibrils, and suprafibrillar structures. J. Struct. Biol. *137*, 2–10.

Julien, S., Peters, T., Ziemssen, F., Arango-Gonzalez, B., Beck, S., Thielecke, H., Buth, H., Van Vlierberghe, S., Sirova, M., Rossmann, P., et al. (2011). Implantation of ultrathin, biofunctionalized polyimide membranes into the subretinal space of rats. Biomaterials *32*, 3890–3898.

Kanai, F., Marignani, P.A., Sarbassova, D., Yagi, R., Hall, R.A., Donowitz, M., Hisaminato, A., Fujiwara, T., Ito, Y., Cantley, L.C., et al. (2000). TAZ: a novel transcriptional co-activator regulated by interactions with 14-3-3 and PDZ domain proteins. EMBO J. *19*, 6778–6791.

Kanchanawong, P., Shtengel, G., Pasapera, A.M., Ramko, E.B., Davidson, M.W., Hess, H.F., and Waterman, C.M. (2010). Nanoscale architecture of integrin-based cell adhesions. Nature *468*, 580–584.

Keller, R., Davidson, L.A., and Shook, D.R. (2003). How we are shaped: the biomechanics of gastrulation. Differentiation *71*, 171–205.

Lamers, E., van Horssen, R., te Riet, J., van Delft, F.C., Luttge, R., Walboomers, X.F., and Jansen, J.A. (2010). The influence of nanoscale topographical cues on initial osteoblast morphology and migration. Eur. Cells Mater. *20*, 329–343.

Lee, M.R., Kwon, K.W., Jung, H., Kim, H.N., Suh, K.Y., Kim, K., and Kim, K.S. (2010). Direct differentiation of human embryonic stem cells into selective neurons on nanoscale ridge/groove pattern arrays. Biomaterials *31*, 4360–4366.

Lenz, M., Goetzke, R., Schenk, A., Schubert, C., Veeck, J., Hemeda, H., Koschmieder, S., Zenke, M., Schuppert, A., and Wagner, W. (2015). Epigenetic biomarker to support classification into pluripotent and non-pluripotent cells. Sci. Rep. *5*, 8973.

Lian, I., Kim, J., Okazawa, H., Zhao, J., Zhao, B., Yu, J., Chinnaiyan, A., Israel, M.A., Goldstein, L.S., Abujarour, R., et al. (2010). The role of YAP transcription coactivator in regulating stem cell self-renewal and differentiation. Genes Dev. *24*, 1106–1118.

McFarlin, D.F., Finn, K.J., Nealey, P.F., and Murphy, C.J. (2009). Nanoscale through substratum topographic cues modulate human embryonic stem cell self-renewal. J. Biomim. Biomater. Tissue Eng. *2*, 15–26.

Nazareth, E.J.P., Ostblom, J.E.E., Lucker, P.B., Shukla, S., Alvarez, M.M., Oh, S.K.W., Yin, T., and Zandstra, P.W. (2013). High-throughput fingerprinting of human pluripotent stem cell fate responses and lineage bias. Nat. Methods *10*, 1225–1231.

Nishioka, N., Inoue, K., Adachi, K., Kiyonari, H., Ota, M., Ralston, A., Yabuta, N., Hirahara, S., Stephenson, R.O., Ogonuki, N., et al. (2009). The Hippo signaling pathway components Lats and Yap pattern Tead4 activity to distinguish mouse trophectoderm from inner cell mass. Dev. Cell *16*, 398–410.

Oakley, C., and Brunette, D.M. (1993). The sequence of alignment of microtubules, focal contacts and actin filaments in fibroblasts spreading on smooth and grooved titanium substrata. J. Cell Sci. *106* (Pt 1), 343–354.

Pan, D. (2007). Hippo signaling in organ size control. Genes Dev. *21*, 886–897.

Pan, D. (2010). The hippo signaling pathway in development and cancer. Dev. Cell *19*, 491–505.

Pan, F., Zhang, M., Wu, G., Lai, Y., Greber, B., Scholer, H.R., and Chi, L. (2013). Topographic effect on human induced pluripotent stem cells differentiation towards neuronal lineage. Biomaterials *34*, 8131–8139.

Qin, H., Hejna, M., Liu, Y., Percharde, M., Wossidlo, M., Blouin, L., Durruthy-Durruthy, J., Wong, P., Qi, Z., Yu, J., et al. (2016). YAP induces human naive pluripotency. Cell Rep. *14*, 2301–2312.

Raghunathan, V.K., Dreier, B., Morgan, J.T., Tuyen, B.C., Rose, B.W., Reilly, C.M., Russell, P., and Murphy, C.J. (2014). Involvement of YAP, TAZ and HSP90 in contact guidance and intercellular

junction formation in corneal epithelial cells. PLoS One *9*, e109811.

Reimand, J., Arak, T., Adler, P., Kolberg, L., Reisberg, S., Peterson, H., and Vilo, J. (2016). g:Profiler—a web server for functional interpretation of gene lists (2016 update). Nucleic Acids Res. *44*, W83–W89.

Richter, A., Valdimarsdottir, L., Hrafnkelsdottir, H.E., Runarsson, J.F., Omarsdottir, A.R., Ward-van Oostwaard, D., Mummery, C., and Valdimarsdottir, G. (2014). BMP4 promotes EMT and mesodermal commitment in human embryonic stem cells via SLUG and MSX2. Stem Cells *32*, 636–648.

Ritchie, M.E., Phipson, B., Wu, D., Hu, Y., Law, C.W., Shi, W., and Smyth, G.K. (2015). Limma powers differential expression analyses for RNA-sequencing and microarray studies. Nucleic Acids Res. *43*, e47.

Schmitt, F.O., Hall, C.E., and Jakus, M.A. (1942). Electron microscope investigations of the structure of collagen. J. Cell. Physiol. *20*, 11–33.

Steger, M., Boes, S., Thilker, S., and Gillner, A. (2014). Measuring method for the interference contrast of multi-beam-interference. J. Laser Micro Nanoen. *9*, 225–229.

Steger, M., Hartmann, C., Beckemper, S., Holtkamp, J., and Gillner, A. (2013). Fabrication of hierarchical structures by direct laser writing and multi-beam-interference. J. Laser Micro Nanoen. *8*, 210–215.

Sun, Y., Villa-Diaz, L.G., Lam, R.H., Chen, W., Krebsbach, P.H., and Fu, J. (2012). Mechanics regulates fate decisions of human embryonic stem cells. PLoS One *7*, e37178.

Sun, Y., Yong, K.M.A., Villa-Diaz, L.G., Zhang, X., Chen, W., Philson, R., Weng, S., Xu, H., Krebsbach, P.H., and Fu, J. (2014). Hippo/YAP-mediated rigidity-dependent motor neuron differentiation of human pluripotent stem cells. Nat. Mater. *13*, 599–604.

Suzuki, K., Bose, P., Leong-Quong, R.Y., Fujita, D.J., and Riabowol, K. (2010). REAP: a two minute cell fractionation method. BMC Res. Notes *3*, 294.

Takahashi, K., Tanabe, K., Ohnuki, M., Narita, M., Ichisaka, T., Tomoda, K., and Yamanaka, S. (2007). Induction of pluripotent stem cells from adult human fibroblasts by defined factors. Cell *131*, 861–872.

Unadkat, H.V., Hulsman, M., Cornelissen, K., Papenburg, B.J., Truckenmuller, R.K., Carpenter, A.E., Wessling, M., Post, G.F.,

Uetz, M., Reinders, M.J., et al. (2011). An algorithm-based topographical biomaterials library to instruct cell fate. Proc. Natl. Acad. Sci. USA *108*, 16565–16570.

Varelas, X., Sakuma, R., Samavarchi-Tehrani, P., Peerani, R., Rao, B.M., Dembowy, J., Yaffe, M.B., Zandstra, P.W., and Wrana, J.L. (2008). TAZ controls Smad nucleocytoplasmic shuttling and regulates human embryonic stem-cell self-renewal. Nat. Cell Biol. *10*, 837–848.

Warmflash, A., Sorre, B., Etoc, F., Siggia, E.D., and Brivanlou, A.H. (2014). A method to recapitulate early embryonic spatial patterning in human embryonic stem cells. Nat. Methods *11*, 847–854.

Willmann, C.A., Hemeda, H., Pieper, L.A., Lenz, M., Qin, J., Joussen, S., Sontag, S., Wanek, P., Denecke, B., Schuler, H.M., et al. (2013). To clone or not to clone? Induced pluripotent stem cells can be generated in bulk culture. PLoS One *8*, e65324.

Wojciak-Stothard, B., Curtis, A., Monaghan, W., MacDonald, K., and Wilkinson, C. (1996). Guidance and activation of murine macrophages by nanometric scale topography. Exp. Cell Res. *223*, 426–435.

Yu, F.-X., Zhao, B., and Guan, K.-L. (2015). Hippo pathway in organ size control, tissue homeostasis, and cancer. Cell *163*, 811–828.

Yu, P., Pan, G., Yu, J., and Thomson, J.A. (2011). FGF2 sustains NANOG and switches the outcome of BMP4-induced human embryonic stem cell differentiation. Cell Stem Cell *8*, 326–334.

Zhao, B., Li, L., Lu, Q., Wang, L.H., Liu, C.Y., Lei, Q., and Guan, K.L. (2011). Angiomotin is a novel Hippo pathway component that inhibits YAP oncoprotein. Genes Dev. *25*, 51–63.

Zhou, Q., Kuhn, P.T., Huisman, T., Nieboer, E., van Zwol, C., van Kooten, T.G., and van Rijn, P. (2015). Directional nanotopographic gradients: a high-throughput screening platform for cell contact guidance. Sci. Rep. *5*, 16240.

Zhou, Q., Wünnemann, P., Kühn, P.T., de Vries, J., Helmin, M., Böker, A., van Kooten, T.G., and van Rijn, P. (2016). Mechanical properties of aligned nanotopologies for directing cellular behavior. Adv. Mater. Inter. *3*, 1600275.

Zou, H., and Niswander, L. (1996). Requirement for BMP signaling in interdigital apoptosis and scale formation. Science *272*, 738–741.

Supplemental Information

Surface Topography Guides Morphology and Spatial Patterning of Induced Pluripotent Stem Cell Colonies

Giulio Abagnale, Antonio Sechi, Michael Steger, Qihui Zhou, Chao-Chung Kuo, Gülcan Aydin, Carmen Schalla, Gerhard Müller-Newen, Martin Zenke, Ivan G. Costa, Patrick van Rijn, Arnold Gillner, and Wolfgang Wagner
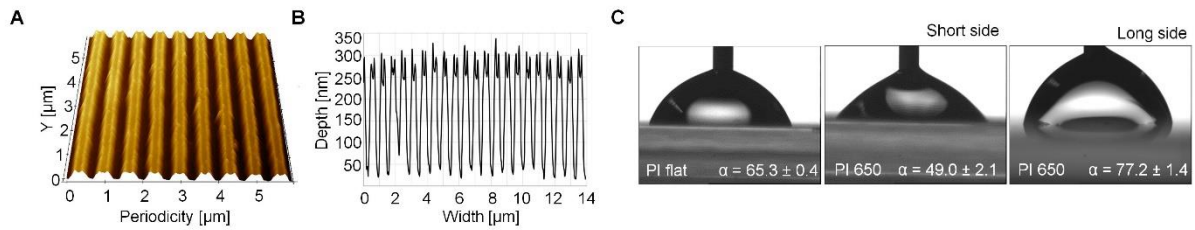
Figure S1. Characterization of sub-microstructured polyimide substrates (relates to Figure 1)
(A) Atomic force microscopy (AFM) image of the polyimide foil featuring sub-micron grooves with a periodicity of 650 nm.
(B) AFM profiles of the grooves show uniform structuring across the substrate. The average depth of the grooves is 200 nm.
(C) Images of water drops on the PI substrates, which were used to assess their hydrophobicity, α indicates the amplitude of the angle that water droplets form when they are in contact with the surface of the material.
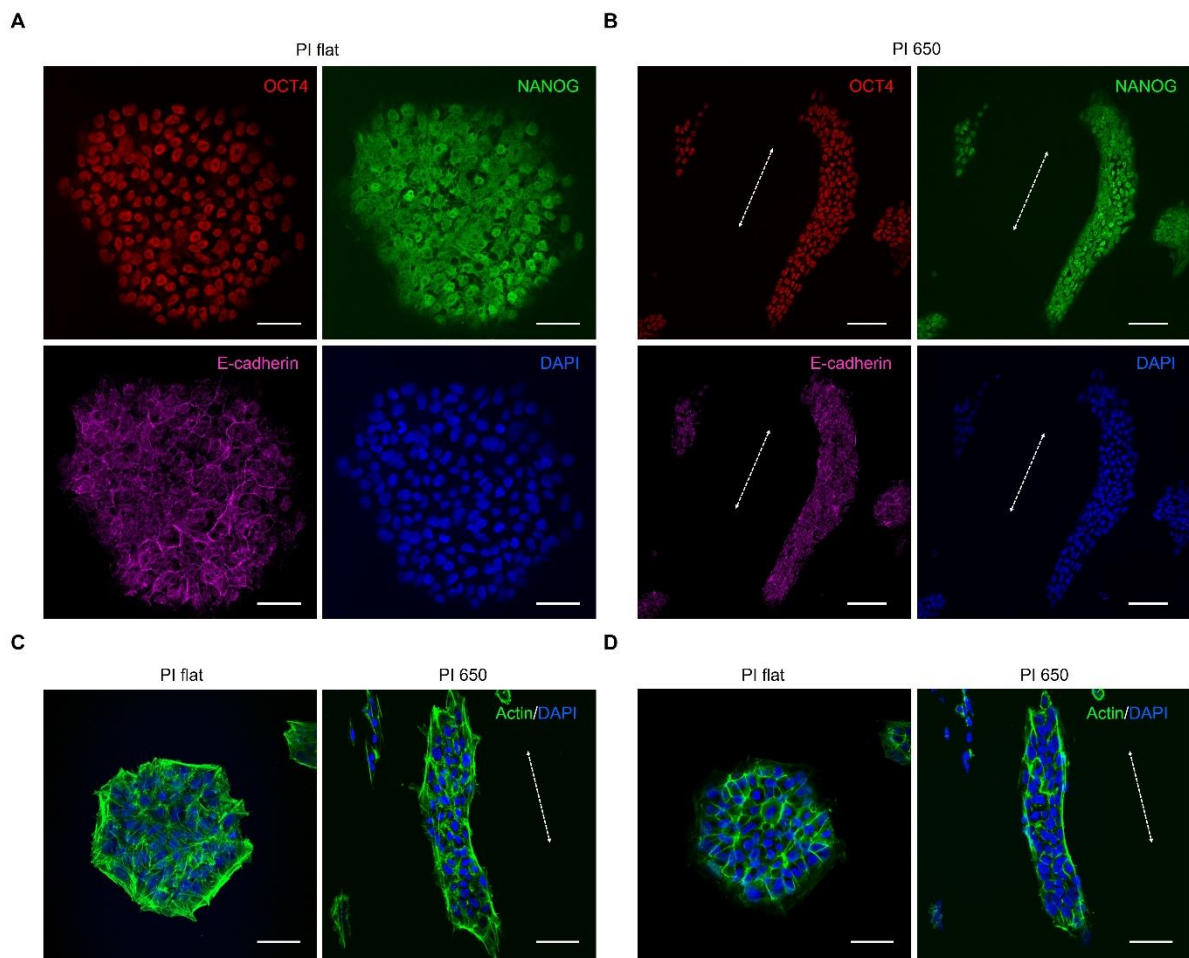

Figure S2. Expression of pluripotency marker and cytoskeletal organization of iPSCs colonies on different substrates (relates to Figure 2)
(A) Immunofluorescence images of iPSCs colonies on flat PI positive for the pluripotency markers OCT4 (red), NANOG (green) and E-cadherin (purple).
(B) Confocal microscopy image showing elongated colonies on PI 650 stained for OCT4 (red), NANOG (green) and E-cadherin (purple).
(C) Confocal microscopy pictures of actin filaments (green) in the basal part of iPSCs colonies.
(D) Confocal microscopy images of the same colonies shown in (C) highlighting the cortical portion of the actin cytoskeleton. Scale bar =50 μm for (A,C,D) and 100 μm for (B). Nuclei are highlighted in blue and the dotted arrows indicate the direction of the grooves.
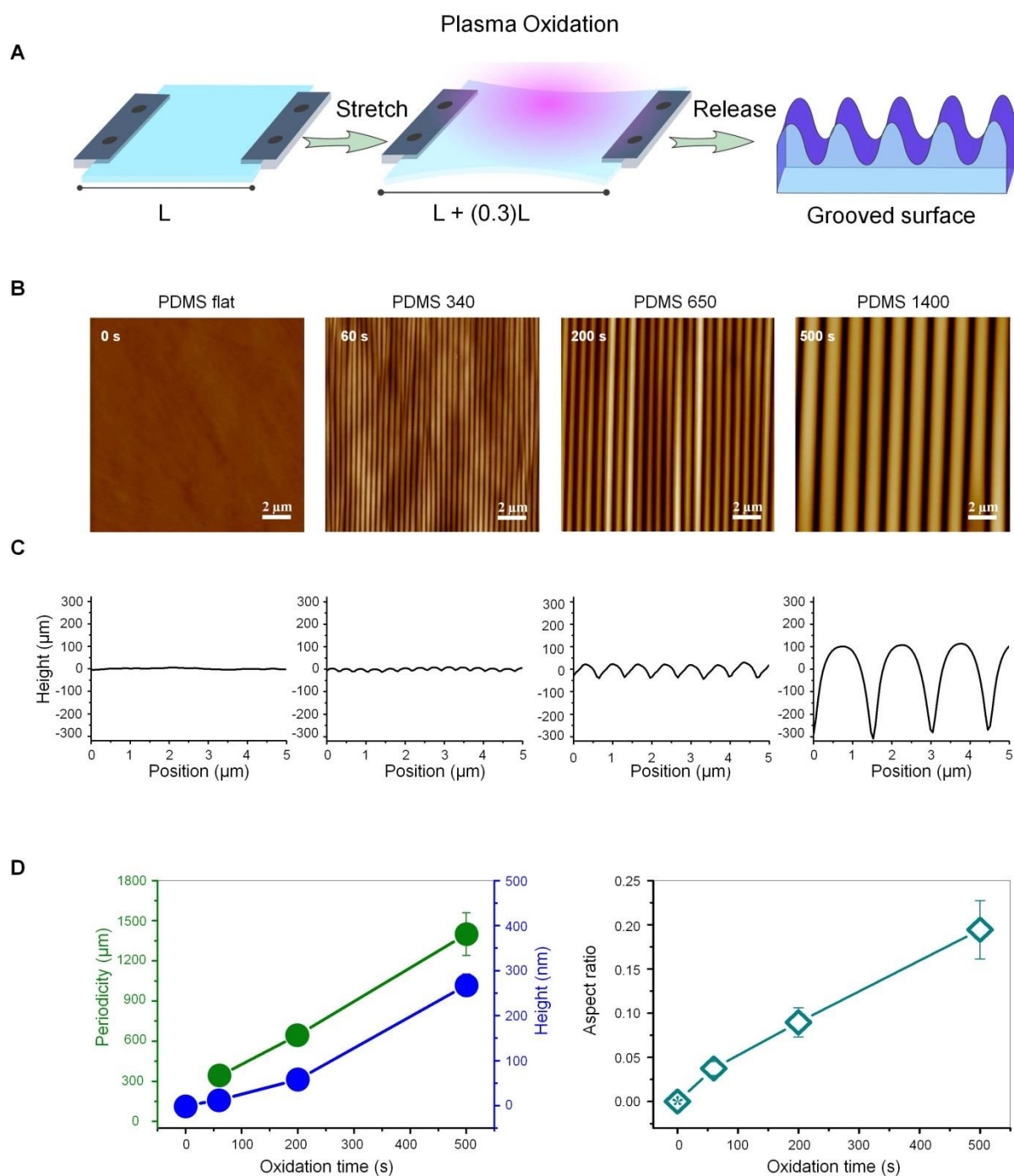
Figure S3. Generation of grooved PDMS substrates (relates to Figure 3)
(A) Schematic representation of the method used to structure PDMS materials with grooves of different dimensions.
(B-C) AFM profiles of the PDMS substrates with grooves featuring periodicities of 340, 650 and 1400 nm. Height and periodicity of the structures increases with increasing exposure time, indicated in seconds. Non-stretched PDMS substrates were used as flat control.
(D) Histograms showing the relation between oxidation time and dimensions of the grooves with regards to both their periodicity and height. Aspect ratio is here defined as the height of the grooves divided by their periodicity.
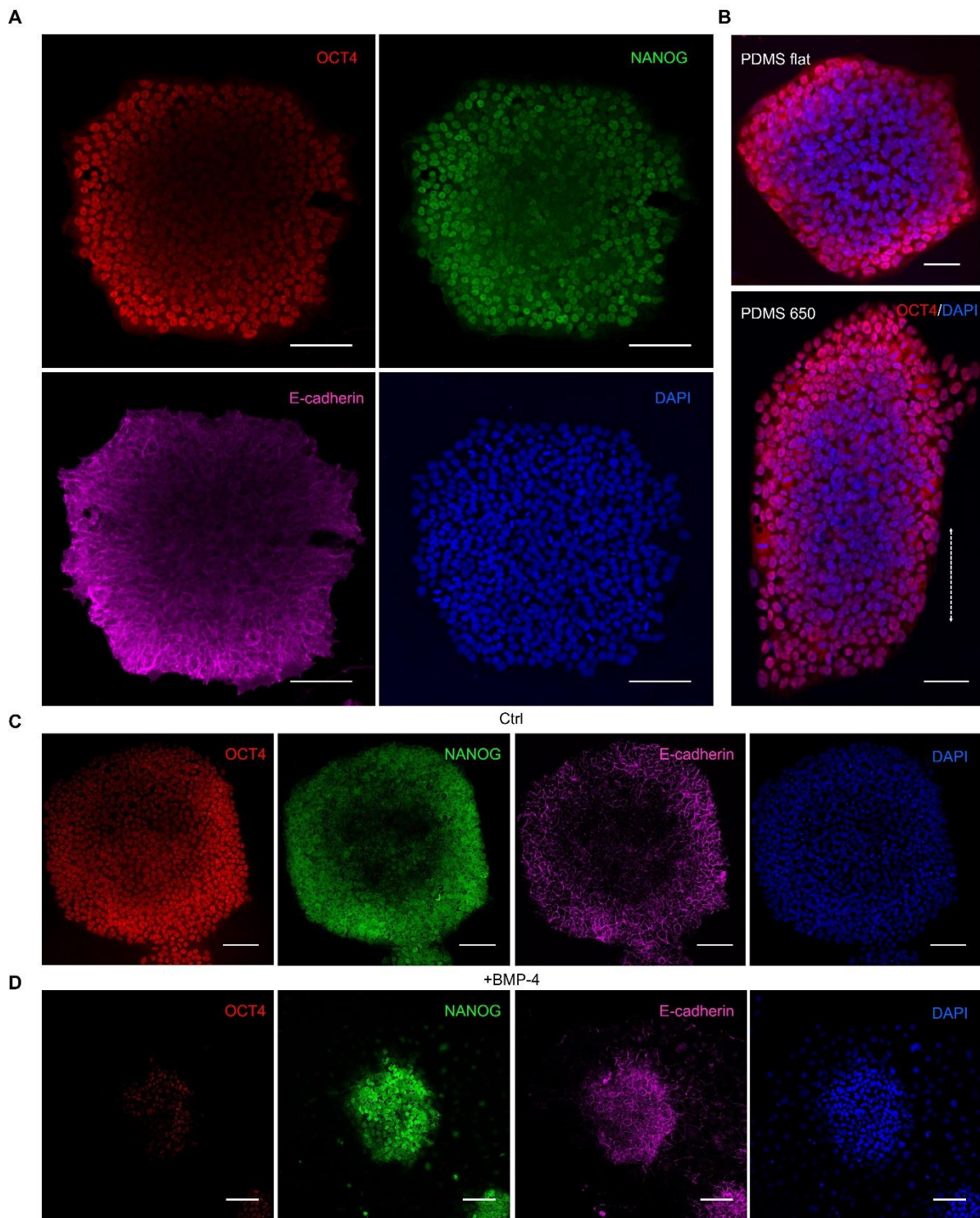
**Figure S4. Spatial distribution of pluripotency markers in iPSC colonies (relates to Figure 4)**
(A) Confocal microscopy images of iPSCs colonies seeded on polystyrene coverslips showing increased expression for OCT4 (red), NANOG (green) and E-cadherin (purple) at the colony rim as compared to the center.
(B) Immunofluorescence images of iPSCs colonies seeded on flat and sub-micron grooved PDMS displaying OCT4 patterning similar to the one observed on the polyimide substrates. The dotted arrows indicate the directions of the grooves; nuclei are stained in blue with DAPI.
(C) Confocal microscopy images of iPSCs in TeSR-E8 medium seeded on PI flat and showing stronger expression of pluripotency markers at the rim as opposed to the center.
(D) iPSCs colonies cultured on PI flat for 48 hours in TeSR-E8 medium supplemented with 50 ng/mL of BMP4 display loss of OCT4, NANOG and E-cadherin starting from the rim and proceeding toward the center. Scale bars = 100 µm for (A,C,D) and 50 µm for (B).

3
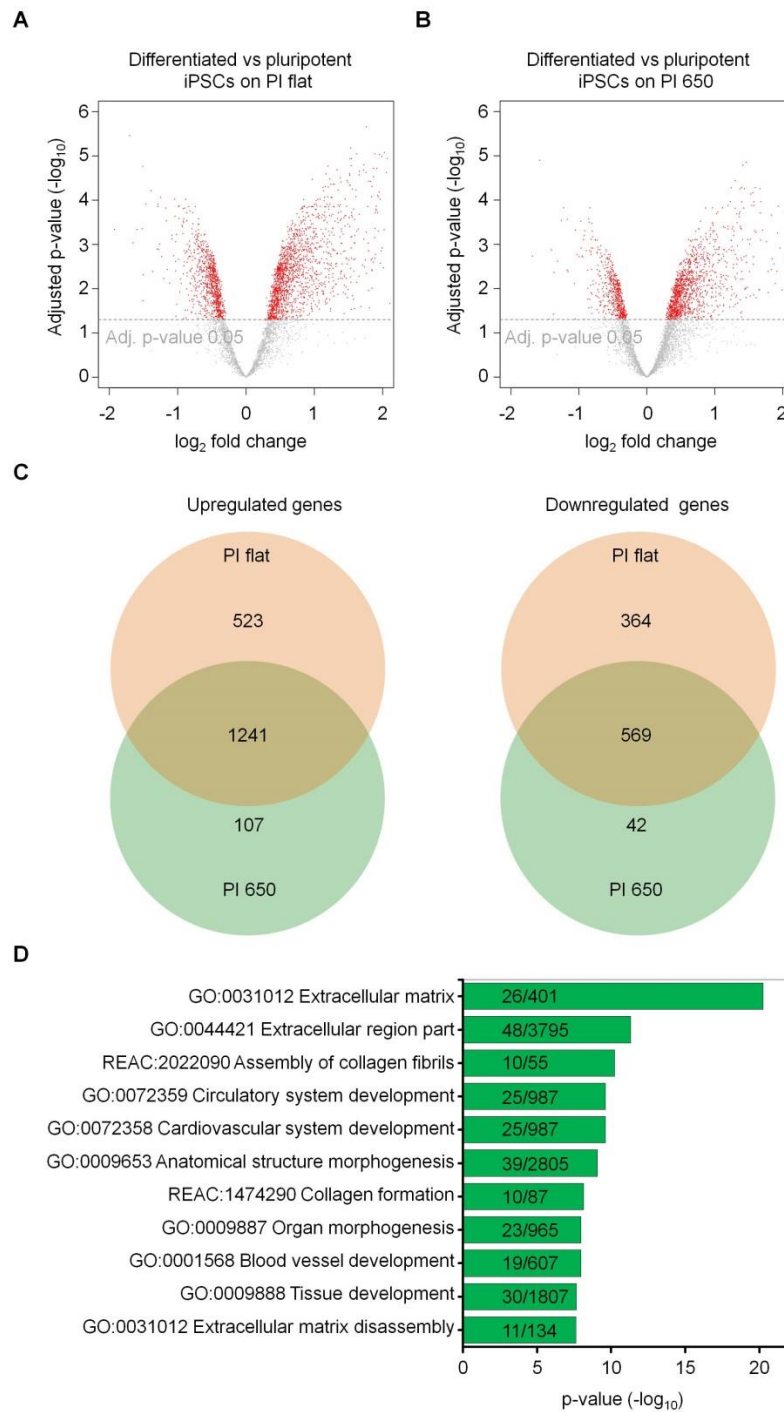
Figure S5. Gene expression changes in iPSCs after differentiation on either flat or grooved polyimide (relates to Figure 5)

(A-B) Volcano plots of differential gene expression upon differentiation of iPSCs on flat PI (A) and structured PI (B) (n = 3 independent biological replica, adjusted p-value < 0.05, paired limma t-test).

(C) Venn diagrams depicting the numbers of significantly up- or downregulated genes (n = 3 independent biological replica).

(D) Differentially expressed genes in iPSCs upon differentiation on PI flat *versus* PI 650 were classified by Gene Ontology categories. Numbers in the bars indicate differentially expressed genes per category and the total number of genes of the category (n = 3 independent biological replica, p values were calculated based on Fisher Exact test followed by multiple test correction as provided by g;profiler). GO = Gene Onthology, REAC = Reactome.
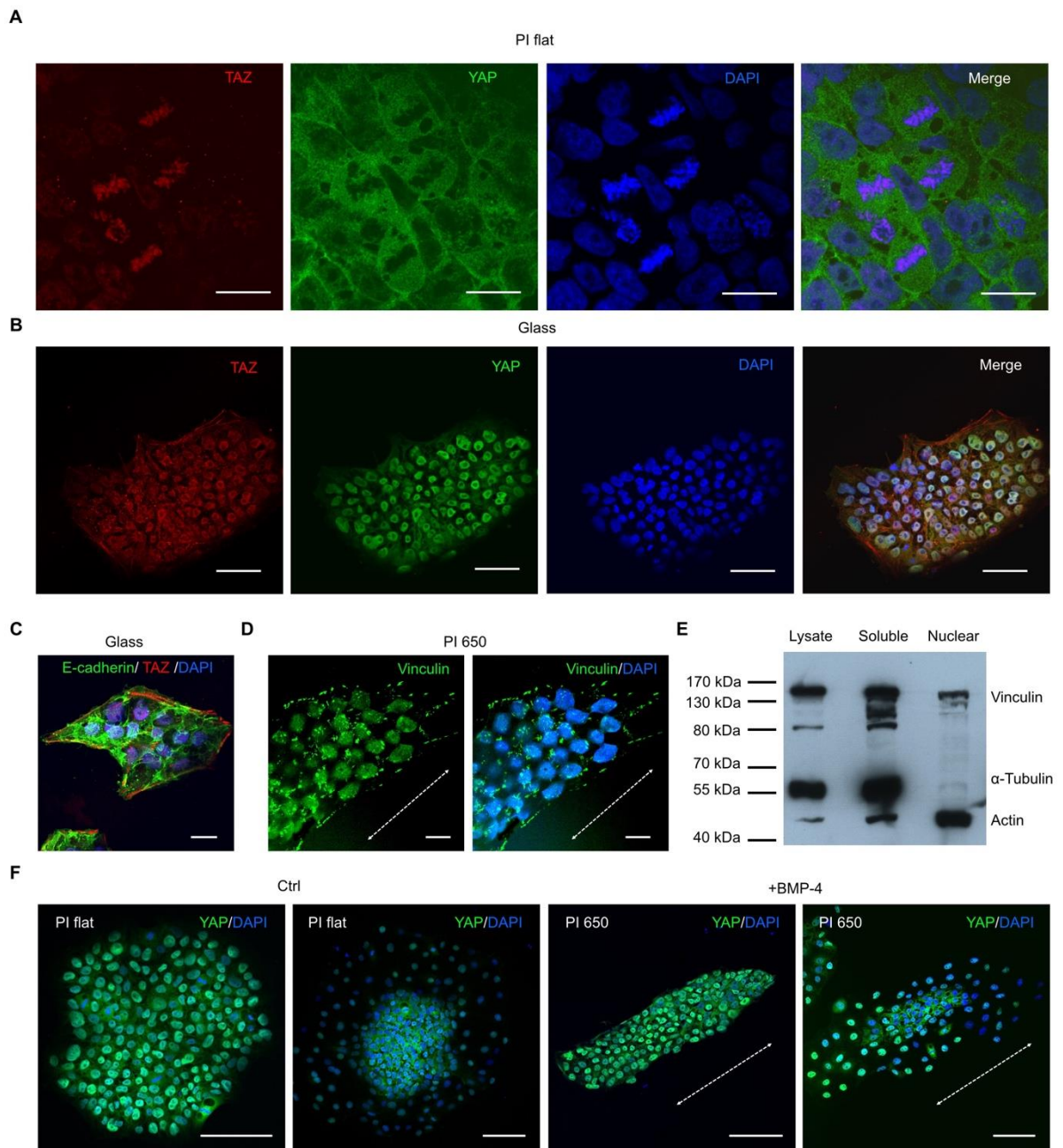
Figure S6. Subcellular localization of YAP and TAZ in iPSC (relates to Figure 6)
(A) Immunostaining of dividing iPSC displaying cytoplasmic distribution of YAP (green) and co-localization of TAZ (red) with the condensed chromatin (DAPI, blue) during mitosis. Scale bar = 10 µm.
(B) Immunofluorescence images showing that TAZ (red) but not YAP (green) is found in filamentous structures. Scale bars = 50 µm.
(C) TAZ filaments were not associated with the cell-cell adhesion molecule E-cadherin (green). Scale bar = 20 µm.
(D) Immunostaining depicts the focal adhesion protein vinculin at adhesion sites as well as in the nucleus of iPSC. The dotted arrows indicate the directions of the grooves. Scale bars = 20 µm.
(E) Western blot analysis of subcellular fractions of iPSC validates that vinculin is partly present in the nuclear fraction, while tubulin is exclusively in the soluble fraction.
(F) Confocal microscopy images of iPSCs cultured in TeSR-E8 showing YAP translocation to the cytoplasm upon BMP4 treatment similarly to what observed for colonies cultured in iPS-Brew. The dotted arrows always indicate the directions of the grooves. Scale bars = 100 µm.

5

Table S1. Differentially expressed genes in differentiated iPSC on PI 650 versus PI flat after 2 weeks of spontaneous differentiation

Affy ID	Gene symbol	Gene name	Mean Expr	log Fold Change	adj.P.Val
TC10001517.hg.1	ANKRD1	ankyrin repeat domain 1 (cardiac muscle)	5.718	-1.269	0.028
TC13000769.hg.1	SLITRK6	SLIT and NTRK-like family, member 6	2.976	-1.052	0.026
TC01001805.hg.1	TGFB2	transforming growth factor, beta 2	5.493	-1.044	0.043
TC20000833.hg.1	TGM2	transglutaminase 2	6.418	-0.934	0.026
TC15001335.hg.1	FBN1	fibrillin 1	6.032	-0.898	0.041
TC03000754.hg.1	CLSTN2	calsyntenin 2	5.513	-0.891	0.041
TC02003743.hg.1	COL3A1	collagen, type III, alpha 1	8.535	-0.891	0.010
TC05000937.hg.1	GABRP	gamma-aminobutyric acid A receptor, pi	7.457	-0.886	0.026
TC15001593.hg.1	ITGA11	integrin, alpha 11	5.588	-0.880	0.041
TC04001226.hg.1	IGFBP7	insulin-like growth factor binding prot. 7	7.785	-0.859	0.026
TC05001714.hg.1	LOX	lysyl oxidase	5.269	-0.859	0.049
TC0X000662.hg.1	VGLL1	vestigial-like family member 1	5.495	-0.858	0.021
TC20000363.hg.1	MMP9	matrix metallopeptidase 9	6.538	-0.839	0.041
TC07002236.hg.1	AQP1	aquaporin 1 (Colton blood group)	5.276	-0.819	0.043
TC01003035.hg.1	VTCN1	V-set domain cont. T cell act. inhibitor 1	7.135	-0.816	0.026
TC18000542.hg.1	ALPK2	alpha-kinase 2	4.784	-0.811	0.037
TC11003000.hg.1	H19	H19, imprinted maternally expr.transcript	8.354	-0.798	0.021
TC17001682.hg.1	COL1A1	collagen, type I, alpha 1	8.109	-0.798	0.021
TC05000682.hg.1	TGFBI	transforming growth factor, beta-induced	6.818	-0.790	0.026
TC10000377.hg.1	ARID5B	AT rich interactive domain 5B (MRF1-like)	7.026	-0.789	0.026
TC13000576.hg.1	POSTN	periostin, osteoblast specific factor	4.174	-0.789	0.022
TC16000454.hg.1	MMP2	matrix metallopeptidase 2	7.651	-0.788	0.022
TC08000508.hg.1	STMN2	stathmin 2	6.325	-0.783	0.045
TC16000455.hg.1	LPCAT2	lysophosphatidylcholine acyltransferase 2	5.719	-0.777	0.043
TC05001970.hg.1	HAND1	heart and neural crest derivatives expr. 1	8.515	-0.772	0.021
TC11000198.hg.1	MICAL2	microtubule ass. monooxygenase, calponin and LIM domain containing 2	5.360	-0.761	0.045
TC12001278.hg.1	ARHGDIB	Rho GDP dissociation inhibitor (GDI) beta	4.437	-0.761	0.024
TC08000167.hg.1	BMP1	bone morphogenetic protein 1	6.633	-0.755	0.026
TC07001559.hg.1	SEMA3C	semaphorin 3C	4.726	-0.737	0.043
TC05002969.hg.1	DAB2	Dab, mitogen-responsive phosphoprotein, homolog 2	6.423	-0.737	0.043
TC09001517.hg.1	TNC	tenascin C	7.061	-0.735	0.022
TC03001651.hg.1	CCDC80	coiled-coil domain containing 80	5.191	-0.720	0.041
TC18000140.hg.1	ASXL3	add. sex combs like transcript.regulator 3	5.283	-0.717	0.022
TC17000118.hg.1	TMEM88	transmembrane protein 88	8.130	-0.709	0.021
TC02002606.hg.1	TFPI	tissue factor pathway inhibitor	6.204	-0.708	0.045
TC01002412.hg.1	IFI6	interferon, alpha-inducible protein 6	6.650	-0.707	0.035
TC13000872.hg.1	COL4A1	collagen, type IV, alpha 1	6.994	-0.699	0.041
TC20000602.hg.1	LRRN4	leucine rich repeat neuronal 4	6.822	-0.699	0.024
TC10001744.hg.1	ADAM12	ADAM metallopeptidase domain 12	4.996	-0.698	0.026
TC07000559.hg.1	COL1A2	collagen, type I, alpha 2	9.691	-0.690	0.026

TC02001086.hg.1	SSFA2	sperm specific antigen 2	5.034	-0.688	0.041
TC0X000750.hg.1	BGN	biglycan	6.114	-0.683	0.022
TC22000248.hg.1	TIMP3	TIMP metallopeptidase inhibitor 3	6.652	-0.681	0.043
TC05001205.hg.1	CDH10	cadherin 10, type 2 (T2-cadherin)	3.949	-0.677	0.041
TC14001138.hg.1	NID2	nidogen 2 (osteonidogen)	6.731	-0.675	0.021
TC09002901.hg.1	S1PR3	sphingosine-1-phosphate receptor 3	6.372	-0.674	0.022
TC04001673.hg.1	PDGFC	platelet derived growth factor C	5.270	-0.670	0.049
TC12001803.hg.1	LUM	lumican	4.614	-0.665	0.028
TC16000378.hg.1	TGFB1I1	transforming growth factor beta 1 induced transcript 1	6.464	-0.659	0.043
TC01003692.hg.1	CSRP1	cysteine and glycine-rich protein 1	6.784	-0.655	0.043
TC02000281.hg.1	EPAS1	endothelial PAS domain protein 1	7.366	-0.654	0.043
TC11002335.hg.1	BACE1	beta-site APP-cleaving enzyme 1	6.018	-0.649	0.026
TC05001986.hg.1	ADAM19	ADAM metallopeptidase domain 19	6.776	-0.648	0.041
TC13000392.hg.1	COL4A2	collagen, type IV, alpha 2	7.177	-0.648	0.043
TC08000456.hg.1	SULF1	sulfatase 1	4.759	-0.640	0.026
TC17000383.hg.1	CCL2	chemokine (C-C motif) ligand 2	5.558	-0.635	0.043
TC15000670.hg.1	LOXL1	lysyl oxidase-like 1	6.582	-0.624	0.038
TC12001275.hg.1	ART4	ADP-ribosyltransferase 4	3.982	-0.624	0.026
TC20000717.hg.1	CST4	cystatin S	5.541	-0.623	0.049
TC15001201.hg.1	ACTC1	actin, alpha, cardiac muscle 1	9.652	-0.621	0.033
TC01002962.hg.1	GSTM3	glutathione S-transferase mu 3	4.138	-0.621	0.043
TC05001151.hg.1	SEMA5A	semaphorin 5A	6.892	-0.618	0.041
TC06001825.hg.1	BMP5	bone morphogenetic protein 5	4.584	-0.617	0.026
TC16001165.hg.1	CDH11	cadherin 11, type 2, OB-cadherin	6.750	-0.611	0.026
TC02002905.hg.1	COL6A3	collagen, type VI, alpha 3	6.317	-0.611	0.026
TC08000770.hg.1	WISP1	WNT1 inducible sign. pathway protein 1	5.312	-0.605	0.035
TC16000660.hg.1	CRISPLD2	cysteine-rich secretory protein LCCL domain containing 2	5.868	-0.600	0.041
TC08001660.hg.1	ST3GAL1	ST3 beta-galactoside alpha-2,3-sialyltransferase 1	5.960	-0.598	0.041
TC13000340.hg.1	MBNL2	muscleblind-like splicing regulator 2	5.782	-0.593	0.041
TC05001366.hg.1	IL6ST	interleukin 6 signal transducer	6.536	-0.591	0.043
TC03001527.hg.1	ADAMTS9	ADAM metallopeptidase with thrombospondin type 1 motif, 9	6.405	-0.585	0.041
TC14000075.hg.1	SLC39A2	solute carrier family 39 , member 2	3.623	-0.585	0.030
TC12001277.hg.1	ERP27	endoplasmic reticulum protein 27	4.623	-0.581	0.043
TC01001623.hg.1	RGS13	regulator of G-protein signaling 13	3.066	-0.570	0.046
TC11001786.hg.1	APLNR	apelin receptor	6.472	-0.564	0.043
TC06001027.hg.1	TNFAIP3	tumor necrosis factor, alpha-ind. protein 3	6.247	-0.560	0.041
TC07001722.hg.1	RELN	reelin	5.318	-0.558	0.035
TC04000158.hg.1	SLIT2	slit homolog 2 (Drosophila)	5.402	-0.550	0.043
TC08001175.hg.1	PLAT	plasminogen activator, tissue	6.520	-0.547	0.043
TC20000134.hg.1	RIN2	Ras and Rab interactor 2	5.474	-0.544	0.043
TC01002292.hg.1	MIR1290	microRNA 1290	3.033	0.626	0.041
TC07001812.hg.1	FEZF1	FEZ family zinc finger 1	6.244	0.821	0.021
TC05000802.hg.1	JAKMIP2-AS1	JAKMIP2 antisense RNA 1	7.185	0.846	0.021
TC06000312.hg.1	OR2J2	olfactory receptor, fam. 2, subf J, member 2	4.980	1.007	0.010

Movie S1. Topography guides cell division polarity (relates to Figure 2)
Phase contrast movie taken over 48 hours of a single iPSC seeded on the sub-micron grooves. The dotted arrow indicates the direction of the grooves. Time is indicated as hours: minutes: seconds.

Movie S2. TAZ shows typical filamentous staining in iPSC (relates to Figure 4)
Z-stack sequence of confocal microscopy images showing an iPSC colony with the TAZ stained in red and the focal adhesion marker vinculin in green. Nuclei are shown in blue.

Movie S3. TAZ-GFP is present in fibrils with iPSC (relates to Figure 4)
Time lapse images taken with Total Internal Reflection Fluorescence (TIRF) of iPSC expressing TAZ-GFP. Fibrillar localization of TAZ is visible at the rim of the colony. Time is indicated as minutes: seconds.

Movie S4. TAZ shuttles to the nucleus during cell division (relates to Figure 4)
Time lapse of iPSC seeded on glass and expressing TAZ-GFP construct. Time is indicated as hours: minutes: seconds.